Graz University of Technology

Institute for Computer Graphics and Vision

Master's Thesis

Pulmonary Vessel Detection and Analysis from CT Images

Michael Helmberger

Graz, Austria, May 2013

Thesis supervisor

Prof. Dr. Horst Bischof

Thesis advisors

Dr. Martin Urschler

Dr. Zoltán Bálint

(Ludwig Boltzmann Institute for Lung Vascular Research)

Für Opa

Abstract

Extraction, segmentation and analysis of pulmonary vessels from computed tomography (CT) images of the human chest is an important topic for a wide range of applications in medical image analysis. We present a pulmonary vessel extraction and segmentation algorithm which is fast, fully automatic and robust against noise. It uses a segmentation of the airway tree and a left and right lung labeled volume to restrict the response of an offset medialness vessel enhancement filter. We test our algorithm on phantom data as well as on the VESSEL12 challenge dataset. Our clinical focus is on the detection of pulmonary hypertension (PH), which is a chronic disorder of the pulmonary circulation, marked by an elevated mean pulmonary arterial pressure (mPAP). On a dataset containing 24 patients from a clinical pulmonary hypertension pilot study, we show that quantitative indices derived from the segmented pulmonary vessels correlate with the mPAP and are applicable to distinguish patients with and without PH.

Keywords. pulmonary vessels, segmentation, fractal dimension, tortuosity, pulmonary hypertension, CT

Kurzfassung

Die Erkennung, Segmentierung und Analyse von Blutgefäßen aus Computertomographie (CT) Aufnahmen ist ein wichtiger Bereich der medizinischen Bildverarbeitung mit zahlreichen klinischen Anwendungsgebieten. Wir präsentieren einen effizienten, voll automatischen und robusten Algorithmus, der Blutgefäße in der Lunge (pulmonale Gefäße) erkennt und segmentiert. Mithilfe eines Vessel-Enhancement Filters, der auf die linke und rechte Lunge beschränkt wird, und unter Einbeziehung von Information aus einer Segmentierung der Bronchien, erkennen und segmentieren wir die pulmonalen Blutgefäße. Wir testen den Algorithmus auf einem Phantombild sowie auf den Datensätzen der VESSEL12 Challenge. Als klinische Anwendung fokussieren wir uns auf die Erkennung von Pulmonaler Hypertonie (PH), einer Erkrankung, die durch einen erhöhten Blutdruck und Gefäßwiderstand im Lungenkreislauf gekennzeichnet ist. Aufgrund von Daten von 24 Patienten, die sich im Rahmen einer klinischen Pilot Studie einer CT Untersuchung unterzogen haben, zeigen wir, dass quantitative Messwerte aus den segmentierten pulmonalen Gefäßen mit dem Lungendruck korrelieren und wir mit unserer Methode Patienten mit und ohne PH unterscheiden können.

Acknowledgments

Over the last year a large number of people influenced and helped me on my way towards achieving the MSc degree. First and foremost, I would like to thank my thesis supervisor Dr. Martin Urschler. Without his guidance and persistent help this master's thesis would not have been possible. I would also like to thank Dr. Zoltán Bálint and DI Michael Pienn from the Ludwig Boltzmann Institute for Lung Vascular Research. Zoltán and Michael introduced me to the clinical part of the thesis, always had an open ear for problems and questions and provided a lot of useful hints.

Most of the work of this Master's thesis would never have been possible without the financial support of the Ludwig Boltzmann Institute for Lung Vascular Research, Graz. Especially I would like to acknowledge Prof. Andrea Olschewski, the head of the institute and Prof. Horst Olschewski for the discussions which had significant influence on my work.

Finally and most importantly I would like to thank my mum, who encouraged me in the first place to begin a study and Veronika, for her love and patience with me during the writing of this thesis.

Statutory Declaration

I declare that I have authored this thesis independently, that I have not used other than the declared sources / resources, and that I have explicitly marked all material which has been quoted either literally or by content from the used sources.

Place	Date	Signature

Eidesstattliche Erklärung

Ich erkläre an Eides statt, dass ich die vorliegende Arbeit selbstständig verfasst, andere als die angegebenen Quellen/Hilfsmittel nicht benutzt, und die den benutzten Quellen wörtlich und inhaltlich entnommene Stellen als solche kenntlich gemacht habe.

Ort	Datum	Unterschrift

Contents

List of Figures

List of Tables

Chapter 1

Introduction

Contents

1.1 Motivation

Since its introduction in the 1970s, computed tomography (CT) has become an important tool in medical imaging. It is the gold standard in the diagnosis of a large number of different disease entities [9, 58], and further technological progress has strengthened its diagnostic impact leading to an essential role in clinical practice. However, with increasing spatial resolution of CT images also the amount of data in CT images increases. Automatic algorithms are needed to give comparable, quantitative data on patients, in contrast to the subjective diagnosis of a radiologist which depends a lot on her or his experience.

In this thesis we present a fully automatic algorithm that is able to detect and segment vessels in the lung (pulmonary vessels). Extraction, segmentation and analysis of the pulmonary vessel tree from CT images is already used for computer aided diagnosis of vascular diseases [53], non-rigid image registration [38], or detection of pulmonary embolism [60]. A depiction of the lung anatomy, the function and a slice from a CT scan is shown in Figure 1.1.

Our clinical interest is on the detection of pulmonary hypertension (PH), which is a chronic disorder of the pulmonary circulation, marked by an elevated mean pulmonary ar-

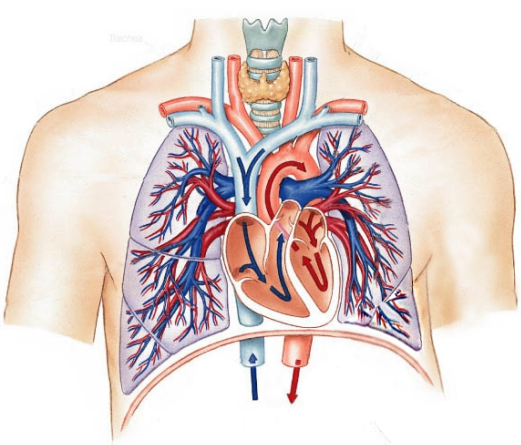

(a)

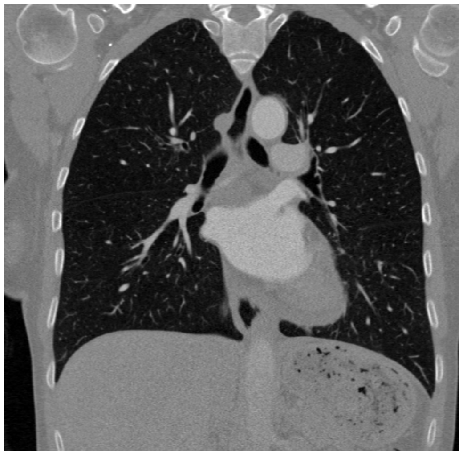

(b)

Figure 1.1: (a) Pulmonary circulation: deoxygenated blood leaves through the right ventricle, through the pulmonary artery to the capillaries where the gas exchange takes place. Blood leaves the capillaries through the pulmonary vein to the heart, where it re-enters at the left atrium (© James W. Clack, www.iupucbio2.iupui.edu/anatomy). (b) Coronal view of the thorax from a CT-image.

terial pressure (mPAP). In healthy people the mPAP is only 12-16 millimeters of mercury, in cases of severe pulmonary hypertension, pulmonary blood pressure can be 3-5 times higher, thus the right heart chamber is overloaded and can fail. Unlike the systematic circulation, the blood pressure in the pulmonary vessels is very difficult to measure. The gold standard for determining the pulmonary pressure is invasive right heart catheterisation (RHC) [18]. Unfortunately PH has usually progressed to late stage by the time of diagnosis. Early PH is often asymptomatic and, by the time symptoms appear, disease progression is well advanced and not reversible [5]. The most common symptoms of PH include shortness of breath, particularly upon physical exercise (exertional dyspnea), fatigue, dizziness and fainting, all of which are worsened by exertion. PH can affect people of all ages, including children, though the average age at diagnosis is 50 years [1]. There are no definitive figures for the prevalence of PH but it is thought that there are several million patients globally. By finding a non-invasive way of measuring the pulmonary blood pressure, the number of patients awaiting treatment could be significantly decreased. Therefore, early diagnosis of pulmonary hypertension is an important aim of clinical research. This thesis was done in cooperation with the Ludwig Boltzmann Institute for Lung Vascular Research, Graz, Austria, where a clinical PH pilot study including 24 patients was conducted.

The following goals were defined for this project:

- Designing an algorithm that can detect vessels inside the lungs without any user intervention,
- finding a readout from the extracted vascular structure that correlates with the mean arterial pulmonary blood pressure,
- creating a fast and efficient implementation of the algorithm, that can be used in daily clinical practice. Further, the algorithm should be able to work on full resolution CT scans (several hundreds of 512x512 pixel slices) to gain full benefit from the available data.

1.2 Related Work

In this section we will give only a short survey of related work, more detailed reviews, ordered by methodological aspects, can be found in the appropriate sections of the thesis.

1.2.1 3D Vessel Segmentation

Several 3D vessel segmentation algorithms have been presented up till now, excellent reviews can be found in [36] and in [30]. In general, existing techniques can be classified into three different classes: vessel detection and segmentation using *appearance and geometric models*, using *image features*, and using *extraction schemes*.

An approach based on an appearance model was done by Boskamp et al. [6], where theoretical knowledge about the vessel intensity distribution was directly applied for vessel segmentation. Frangi et al. [15, 17] published works that rely on implicit geometric assumptions on the vessel surface. Frangi et al. [14] also published a method based on image features, namely second-order derivative information derived from the Hessian matrix. This method relies on the eigenvalues and vectors of the Hessian matrix to discriminate between plane-, blob- and tubular-like structures. As an alternative to Hessian based filters, Bauer and Bischof [3] used the gradient vector flow and the local Jacobian to find tubular structures. Another approach to vessel segmentation are region growing techniques. They fall in the category of greedy algorithms, employ low-level, simple inclusion rules, and explore datasets only sparsely, a critical advantage for large 3D datasets. Region growing based techniques can be distinguished between classical region growing [6], and wave propagation techniques [7]. A more accurate, yet still computationally efficient

alternative for the wave propagations is the fast-marching algorithm [52], as a special case derivation of general level-set approaches. Extraction schemes combine geometric models and image features, together with pre-processing and pre-segmentation steps to simplify image content.

Our vessel detection and segmentation approach is inspired by the commonly used Hessian based filters, combined with an active contour model.

1.2.2 Non-Invasive Detection of Pulmonary Hypertension

Regarding the non-invasive detection of PH, two previous works have been published. It was shown that the fractal dimension (FD) of the pulmonary vessel tree of children suffering from pulmonary hypertension correlates with the pulmonary vascular resistance [42]. Moreover, in their study, lower FD was associated with poorer survival. In another study, it was presented that an increase in the two dimensional FD of the pulmonary arteries in PH patients, was highly correlating with the pulmonary blood pressure [23]. However, these two studies used maximum intensity projections (MIP) of the vessel trees to compute the FD, whereas we hypothesize that quantitative readouts need to be performed on 3D voxel data.

1.3 Overview and Contributions

The focus of this work is on the robust segmentation of the pulmonary vessel tree and on the structural analysis of the obtained tree. For vessel detection, we propose an algorithm that uses a combination of lung- and airway segmentation, together with a sophisticated vessel enhancement filter to obtain a proper segmentation of the left and right pulmonary vessel trees separately, even in patients showing severe pathologies. The algorithm is fully automatic, computationally efficient and able to handle large datasets.

We use an improved version of the vessel enhancement filter proposed by Pock et al. [48], which itself is an extension of the model based approach of Krissian et al. [31], and include additional information derived from airway- and lung-segmentation in the vessel detection and segmentation process. For our algorithm to be used in clinical daily routine, all filters are implemented in CUDA. CUDA is a parallel programming model from NVIDIA, that generates hardware accelerated instructions for NVIDIA graphics processing units (GPUs). Using CUDA we can significantly improve the run time of our 3D image processing algorithms, due to the high degree of parallelization.

From the point of view of the clinical application, we are not aware of anybody computing the 3D fractal dimension of lung vessels before. Also the tortuosity readout of human pulmonary vessels has not been mentioned in the literature.

1.4 Structure of the Thesis

The thesis is organized as follows. In Chapter 2, we give an overview of the vessel extraction algorithm and then explain airway-, lung- and vessel segmentation in detail.

In Chapter 3 we apply the proposed algorithm on three different datasets: a liver vessel tree phantom, 20 publicly available CT scans from the VESSEL12 challenge, and 24 datasets from patients from the clinical PH study.

In Chapter 4 two different readouts of the vascular tree, the fractal dimension and the distance metric, are introduced and computed on the vessel centerlines of the clinical PH study datasets. In Chapter 5 we correlate these readouts with actual clinical parameters from the patients derived from right heart catheterization.

We conclude the work in Chapter 6 and Appendix A shows a list of publications as an outcome of this master's thesis. Appendices B and C describe required implementation dependencies and characteristics of the PH patients.

Chapter 2

Detection and Segmentation of Pulmonary Vessels

Contents

In this chapter we introduce the method for detecting pulmonary vessels, a flowchart of the algorithm is shown in Figure 2.1. The input for the algorithm are contrast enhanced thorax CT scans. We begin with identifying the lung regions through simple thresholding and by segmenting the airways with an iterative region growing algorithm.

Inside the two lungs, we compute the response (i.e. medialness) from a multi-scale vessel enhancement filter (VEF). The VEF is using the eigenvectors of the Hessian matrix, which give information about the local image structure, to detect tubular structures such as vessels. To improve accuracy and robustness against noise, at each position an offset-medialness boundary measure perpendicular to the estimated vessel direction is evaluated [31] and combined with the gradient magnitude at the current position [48]. This gives the final medialness response.

After non-maxima suppression of the medialness, centerlines of the vessels are detected and connected by applying a shortest path algorithm. A coarse vessel segmentation is done by estimating the radius for each vessel centerline point using a spherical ray-casting approach. The final segmentation takes the image edges into account using a globally optimal geodesic active contour model based on total variation [50].

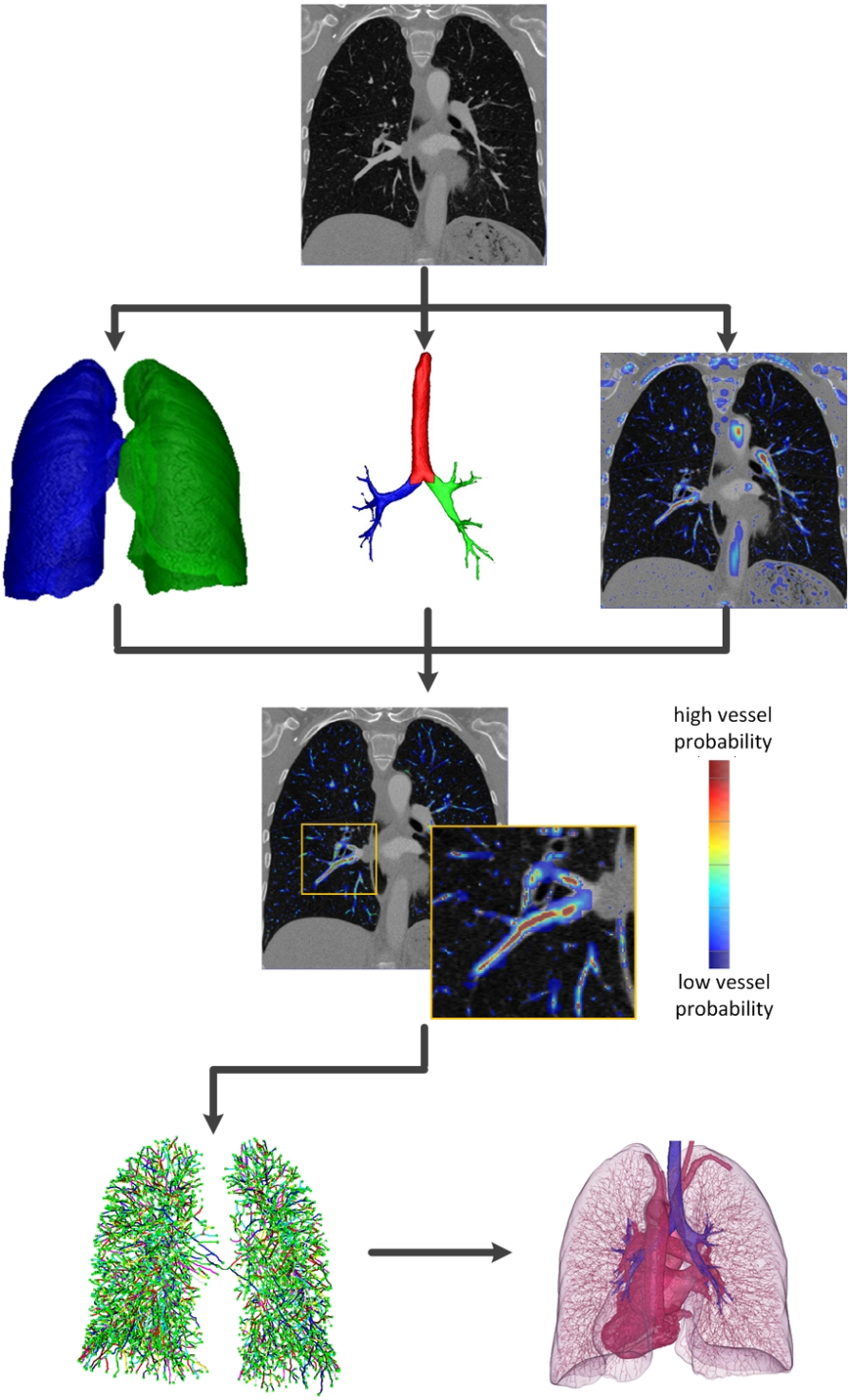

Figure 2.1: Vessel detection flowchart. First row: CT image, second row: lung segmentation, airway segmentation and CT-image with medialness overlay, third row: medialness restricted to the lungs, last row: connected centerlines and 3D rendering of lungs, airways, vessel centerlines and heart.

2.1 Automated Airway Segmentation

Segmentation of the airways is crucial for various clinical applications, such as image-guided peripheral bronchoscopy [22] or the detection of airway related diseases, like asthma and chronic obstructive pulmonary disease [49]. A large number of methods proposed in the literature rely on region growing algorithms, because they are fast and assume no prior knowledge of the shape or size of the airways. Broad overviews of existing methods have been published during the *Extraction of Airways from CT 2009* (EXACT'09) challenge in [37] and in [30, 55]. Our approach uses a simple iterative region growing algorithm since we do not need the whole airway tree for our subsequent steps.

One reason for the airway segmentation is to be able to separate the lung segmentation into left and right lung. Segmentation of the main bronchi is sufficient for this task. A second reason is, that the bronchi usually run along the pulmonary vessels and are attached to it. Since the intensity contrast of the airway border and the blood vessels is very low, we found that incorrect segmentation of the blood vessels can occur. Also here a rather coarse segmentation of the first few generations is sufficient to remove these mistakes. For small bronchi, the airway wall is naturally attenuated due to the partial volume effect.

In this section we first describe the anatomy of the airways, how to automatically detect a seed point for an iterative region growing algorithm, and how we improve the obtained coarse airway segmentation using responses from an airway enhancement filter. This is then followed by a geodesic active contour segmentation step, which leads to the final airway segmentation.

2.1.1 Morphology of the Respiratory Tract

The human respiratory tract is divided into 3 main parts:

- upper respiratory tract (nose, nasal passages, paranasal sinuses, and throat)
- respiratory airways (voice box, trachea, bronchi, and bronchioles)
- lungs (respiratory bronchioles, alveolar ducts, alveolar sacs, and alveoli)

The airways are organized as a branching network of tubes that become narrower, shorter, and more numerous as they penetrate deeper into the lung. We are interested in the airway tree starting with the trachea. At the carina the trachea splits into left and right main bronchi (Figure 2.2). From there on it ramifies into a tree with $\sim$ 17 million branches

with a total surface area of 130 m^2 [20]. Each terminal branch ends in an alveolus where the gas exchange takes place.

In our CT images only airways with a diameter of about 3 mm are clearly distinguishable, the limited resolution and the resulting partial volume effect makes it impossible to detect smaller airways.

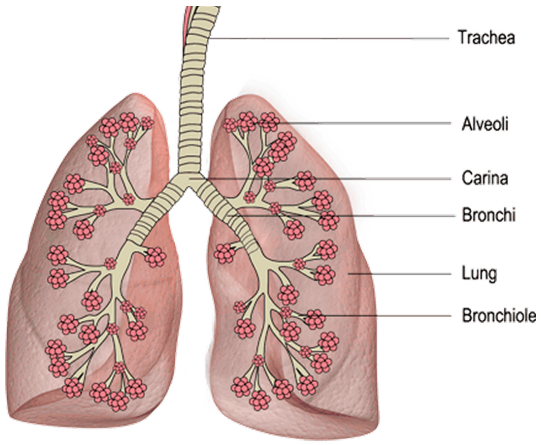

Figure 2.2: Anatomy of the human airway (©EMT-National-Training.com)

2.1.2 Coarse Airway Segmentation

To get rid of some of the noise, two preprocessing steps are performed on the chest CT scan. First, all voxels with a Hounsfield unit (HU) value bigger than -400 HU are clamped [22]. This is the input for our *airway-enhancement filter*. The airway-enhancement filter is the same as the vessel-enhancement filter (see Section 2.3.4), but with enhancement of dark tube-like structures instead of bright tube-like structures. We automatically detect the airway on the top-most slice of the contrast-enhanced volume, which is a dark circle surrounded by high-intensity tissue, to get a seed point $\mathbf{x_s}$ for an iterative 3D region growing algorithm. For the region growing two thresholds are defined: $th_{min} = I(\mathbf{x_s}) - 1$ and $th_{max} = I(\mathbf{x_s}) + 1$, where $I(\mathbf{x})$ is the HU value at position $\mathbf{x}$. All N_6 connected voxels which fulfill

$$th_{min} < I(\mathbf{x}) < th_{max}$$

are added to the segmentation. Then the thresholds are updated ($th_{min} = th_{min} - 1$ and $th_{max} = th_{max} + 1$) and region growing is restarted iteratively with the previous segmentation as seed. This is repeated until leakage of the region growing algorithm is detected. After leakage has occurred, the thresholds from the previous iteration step are

selected as final threshold.

Two measures are monitored for leakage detection: first, if the number of voxels added in the current iteration is 3 times larger then the average number of voxels added at the previous iterations, the region growing is stopped. The second measure is the number of edge voxels. If the number of edge voxels in one iteration is 3 times larger than the number of edge voxels in the previous iteration, the region growing is stopped. To prevent early termination of the region growing algorithm, a minimum volume $V_{min} = 20000\,mm^3$ is introduced. We empirically chose this value under the assumption, that every human airway tree will be larger than this volume V_{min}. For post processing 3D hole filling is applied. In Figure 2.3 the different steps of the region growing as well as a leaked segmentation is shown.

These steps lead to a coarse segmentation of the airway tree. To improve it, we use the tube detection response for airway enhancement in addition to the coarse region growing result and formulate a geodesic active contour to snap to image gradients. This step is inspired by the TVSeg algorithm [59] and the work in [50].

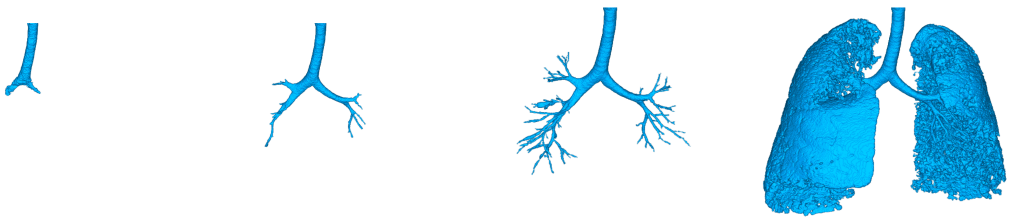

(a) (b) (c) (d)

Figure 2.3: Airway segmentation example: (a) Segmentation after 35 iteration, (b) after 130 iterations, (c) final segmentation after 260 iterations, (d) leaked segmentation.

2.2 Automated Lung Segmentation

Lung segmentation is a crucial step in various tasks related to analysis of the lung. In our case we use it to identify a region of interest for the later pulmonary vessel detection.

In this section an automatic lung segmentation algorithm which separates the two lungs is proposed. It uses a thresholded CT image as coarse lung segmentation and refines it in multiple steps. For the separation into right and left lung, the segmented airway tree is used (see Section 2.1).

2.2.1 Morphology of the Lung

The human lung is subdivided into five lobes that are separated by pulmonary fissures. There are three lobes in the right lung, namely upper, middle, and lower lobe. The right upper and right middle lobes are divided by the right minor fissure, whereas the right major fissure delimits the lower lobe from the rest of the lung. The left lung is usually a little bit smaller than the right lung. It has the cardiac notch which is produced to accommodate the space taken up by the heart and it has only two lobes (upper and lower) that are divided by the left major fissure (Figure 2.4). Together, the lung lobes contain approximately 2,400 kilometres of airways and 300 to 500 million alveoli, having a total surface area of about 70 square metres in adults - roughly the same area as one side of a tennis court [45]. The entire organ weighs about 2.3 kilograms.

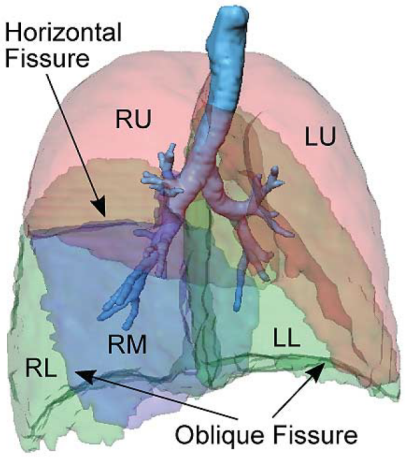

Figure 2.4: Rendering shows the lung subdivided into right upper (RU), right middle (RM), right lower (RL), left upper (LU), and left lower (LL) lobe [35].

2.2.2 Previous Work

Significant amount of previous work has been done on lung segmentation [55]. An overview can be found in the results from the *LObe and Lung Analysis 2011* (LOLA11) challenge*. Most of these algorithms struggle with pathological cases where lung diseases change tissue density. High density pathologies are often connected to the lung border and distort the segmentation. An algorithm based solely on intensity thresholding will not work for these cases. The method from Hu et al. [24] is based on a grey level thresholding of CT images

*http://www.lola11.com/

and uses morphological operations to close holes in the segmentation caused by vessels. In [27] anisotropic diffusion is used as a preprocessing step followed by morphological operations. Another approach described in [28, 33] uses an active contour model additionally to the thresholding segmentation, which leads to a smooth segmentation that includes the artefacts at the lung border and implicitly leads to a separation of the two lungs. The algorithm proposed in [25] uses a graph search driven by a cost function combining the intensity, gradient, boundary smoothness, and the rib cage information.

Our method is based on thresholding and morphological closing. We found that this approach lead to accurate results on our datasets and could be implemented very efficiently. However, the two lungs always merge through the airways and in some datasets the border between right and left lung is hardly visible, resulting in additional connections between the lungs (see Figure 2.5a). This is of course not desirable and thus requires an additional step for separating left and right lung. We propose a novel Dijkstra [10] based method for lung separation.

2.2.3 Left and Right Lung Segmentation Algorithm

First the optimal threshold to separate foreground (body) and background (air) from the thorax CT image is calculated using Otsu's method [46]. With a connected component analysis, the background region which corresponds to the lungs is selected and a 3D hole filling is applied. This leads to one big region for right and left lung, since the two lungs always merge through the airways (and in some patients additional connections of the lung occur because the border between right and left lung is hardly visible, Figure 2.5a). To separate left and right lung, the airway segmentation is used. We detect the carina in the airway segmentation (where the trachea separates into the left and right main bronchi) and assign different labels to the trachea, right and left airway tree. Carina detection works by slice wise scanning of the airway segmentation from top to bottom until we get two independent connected components in the 2D axial slice. If both connected components are connected to the main airway stem in the previous slice, the carina is found.

To label the voxels in the lung mask according to left and right lung, a modified form of Dijkstra's shortest path algorithm [10] is used. For each voxel belonging to the lung mask we calculate the minimum cost path to the trachea. The first label (either right or left airway tree) that lies on this path determines the label of the voxel. As cost function I_c we use the scaled gradient magnitude of the CT image $|\nabla I|$ and the binary lung segmentation I_{lung} excluding the airways I_{airway}

$$I_c = \frac{I_{lung} - I_{airway} + 4 \cdot |\nabla I|}{5}$$

The gradient image $|\nabla I|$ is normalized to be in the interval $[0 \dots 1]$. The scaling factor was empirically found to perform well on our datasets. This enables the lung segmentation to snap onto the border between the two lungs (Figure 2.5b).

As final step, to remove the holes caused by vessels and other high intensity structures, the airways are removed from the lung segmentation and morphological closing is applied at each lung separately. We use a six-neighbourhood star-shaped structuring element and 10 closing operations. The different steps of the lung segmentation can be seen in Figure 2.5. A problem common to all lung segmentation approaches is patients with diseases that cause tissue changes in the lung parenchyma, resulting in high density tissue. Figure 2.6 depicts a patient with severe scleroderma (an autoimmune disease characterized by hardening of the parenchyma and thus making it more dense), where the lung mask does not cover the whole lung.

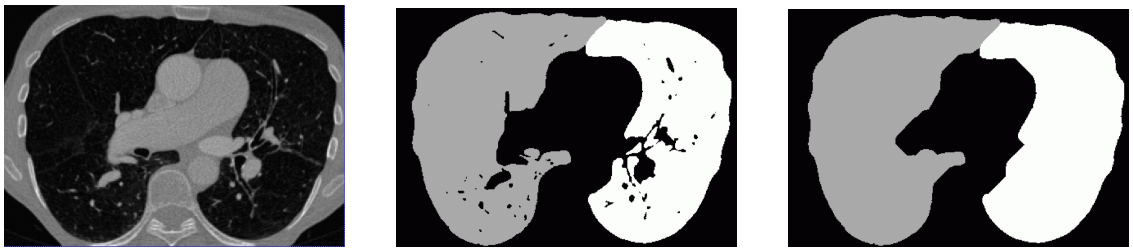

(a) (b) (c)

Figure 2.5: (a) CT image, axial slice, (b) coarse lung segmentation after separation, (c) refined lung segmentation.

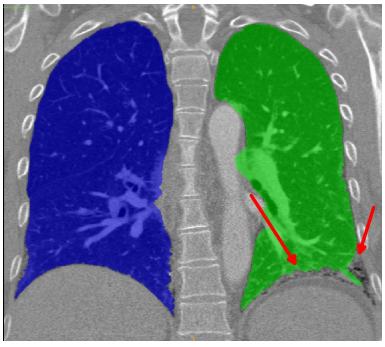

Figure 2.6: Due to the high degree of lung involvement from a scleroderma patient, the segmentation does not cover the whole lung.

2.3 Pulmonary Vessel Segmentation

This section will cover one of the major aims of the thesis, the detection and segmentation of pulmonary vessels. At the core of our method is a multi-scale vessel enhancement (VE) filter based on the Hessian matrix. It is similar to [48] in using the eigenvectors of the Hessian matrix to detect candidate voxels inside the vessels and computing an offset-medialness boundary measure perpendicular to the estimated vessel direction [31]. The VE response (i.e. medialness) is limited to the right and left lung using the lung segmentation from Section 2.2. A non-maxima suppression of the medialness inside the lungs leads to centerline candidate points. Small centerline fragments (less than 5 connected voxels) are removed before a Dijkstra-like shortest path algorithm is used to connect the fragments into a single vessel tree. The vessel radius is estimated at each centerline voxel using a spherical ray-casting approach. The final segmentation is the output of a globally optimal geodesic active contour model based on total variation [50].

2.3.1 Morphometry of Pulmonary Vasculature

The pulmonary vasculature carries deoxygenated blood away from the heart, to the lungs, and returns oxygenated blood back to the heart. The main pulmonary artery extends from the right ventricle of the heart and branches into left and right pulmonary arteries, which branch out into the five lobes of the lung. Pulmonary arteries carry deoxygenated blood to the lung capillaries, where it releases carbon dioxide and binds oxygen during respiration. Blood leaves the capillaries to the pulmonary veins, reaching the heart, where it re-enters at the left atrium. On average, a single blood cell takes roughly 30 seconds to complete a full circuit through both the pulmonary and systemic circulation. In Figure 2.7 the whole circuit is depicted. A typical human lung includes in the order of hundreds of thousands of arterial and venous vessels. Huang et al. [26] found a total 15 generations of arteries and veins between the main pulmonary artery/vein and the capillaries, with diameters varying from 15 mm to 0.02 mm. In our CT images we can recognize vessels down to a diameter of approximately 2 mm, smaller vessels cannot be detected due to the partial volume effect.

2.3.2 Previous Work

Several 3D vessel segmentation algorithms have been presented up till now, some excellent reviews can be found in [36] and in [30]. In [44] they propose a framework that links

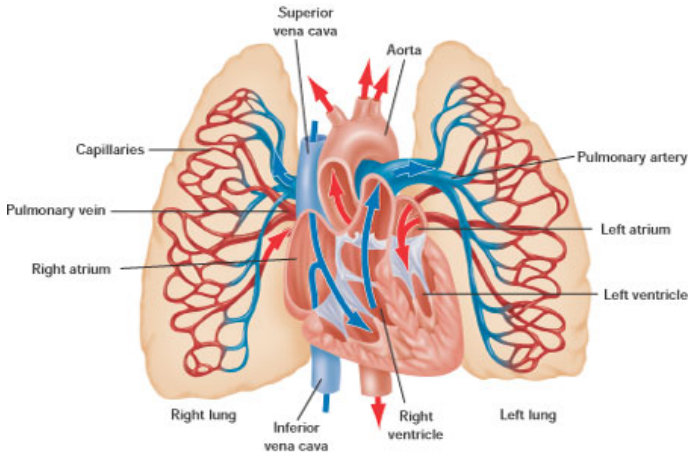

Figure 2.7: Blood circulation in the lungs. Pulmonary veins depicted in blue, arteries in red (Figure © McGraw-Hill Ryerson).

vessel segments based on an iterative process. They take the distance, the angle between segments and a cost function calculated by a kNN classifier into account; first segments with small distance d and similar angle get connected, then the distance is successively increased until a maximal distance (d_{max}) is reached. Each segment is added to the final graph if the cost function (which is based on 12 features such as length of the segment, average grey value, standard deviation of the grey value, curvature,...) is below a threshold t_c. To find the optimal path between segments, dynamic programming is used. When the maximum distance d_{max} is reached, a connected component analysis is performed and the largest component is selected to be the final result. Estrada et al. [11] is using a single source - multiple destination version of Dijkstra's shortest path algorithm to create a vascular forest from the vascular network in the human retina, however only on 2D images. For creating a graph, each candidate pixel (obtained from a vessel enhancement filter) is considered as a node v with arcs e to all 8 neighbouring nodes. The cost of each arc is chosen such that it is high if one or both endpoints are outside the vessel and low if both are inside. With the Dijkstra algorithm it is possible to compute the minimum cost path between any two nodes. An exploratory version of the Dijkstra algorithm is used, which includes every path from the source node to any other node below a certain threshold τ. This algorithm is applied to every candidate pixel. As a result, a forest with shortest path trees is obtained. A slightly different idea utilizing the Dijkstra algorithm is shown in [47]. They also generate a set of seed points, based on a vessel enhancement filter. For each seed point x_0, with its given branch orientation, an optimal path from x_0 to every point on the surface of a sphere of a certain radius is computed. This path is computed via

the Dijkstra algorithm based on a cost function F. From this list of candidate paths, only those that satisfy certain geometrical criteria are selected and added to the final forest. A disadvantage of this method is that due to its locality it does not yield one connected tree. An approach trying to globally optimize the vascular tree is presented in [29]. They utilize high-level prior knowledge (the *minimum flow resistance with minimum vascular volume*) in their approach. The main idea is that the vascular system has to fulfill the perfusion task with minimum effort for maintaining its anatomical structure. They present a cost function that models the tree geometry, the perfusion resistance from the root of the tree to a cell group and the blood flow resistance within the vessels. They further propose a simplified cost function, that consists of a minimum spanning tree and a shortest path tree, and an algorithm to efficiently minimize it. However, even the simplified version of the cost function is difficult to implement, and numerous parameters have to be estimated. A more pragmatic approach is presented in [57] where they first compute a forest (i.e. a graph with no loops) from a given set of vessel-candidate points. This forest is subsequently cleaned and improved using simple geometric filters. Short branches are trimmed and gaps between vessels that geometrically fit to each other are filled in. For constructing the forest Kruskal's minimum spanning tree algorithm is used to subsequently add new branches to a tree sorted by increasing branch length. After the forest is cleaned up, the user selects the root of one tree which is then cleaned up using two simple geometric heuristics: vessels which cause sharp turns in the blood flow directions are removed and vessels which are well aligned but belong to a different tree (for example veins and arteries), are removed by analysing the alignment between a path in the selected tree and the whole forest.

Our proposed reconnection algorithm tries to combine ideas from the approaches mentioned above. We chose to use a shortest path algorithm that takes gradients and the medialness into account.

2.3.3 Preprocessing

Implants like pacemakers or other metallic objects cause extremely high HU values because of their high x-ray attenuation. To reduce this effect, we clamp the input image $I(\mathbf{x})$, which has an original range between $-1024\,\mathrm{HU}$ and $3071\,\mathrm{HU}$, to a maximum HU value of 1500 and scale it to be in the interval $[0, 1]$:

$$I_c(\mathbf{x}) = \max\left(0, \min\left(1, \frac{I(\mathbf{x}) + 1024}{1500 + 1024}\right)\right)$$

To smooth the CT image without blurring the edges we use the Rudin-Osher-Fatemi (ROF) algorithm [51] .

2.3.4 Vessel Enhancement

Vessel detection is based on a modified version of the vessel-enhancement filter (VEF) proposed by Pock et al. [48], an algorithm that was also investigated in the PhD thesis of Christian Bauer [2] to detect liver vessels. The VEF uses the eigenvalues of the Hessian matrix to determine candidate vessel voxels, followed by a combined offset- and center-medialness function to compute the vessel probability. To achieve a reasonable run time of the filter, we implemented it in CUDA. Detecting vessels of different sizes requires the use of multi-scale image pyramids. We use a scale space with 4 scales and a downsampling factor of 1.7 between neighbouring scales. The variance σ_i in voxels for the Gaussian smoothing at each scale i is computed the following way:

$$\sigma_i = \left(\frac{2^{i-1}}{2}\right)^2$$

The use of first and second derivative kernels from [13] (Table 2.1) and the reduced downsampling factor showed improved discrimination between different vessel radii, compared to the widespread use of Gaussian pyramids with a downsampling factor of two. Limited memory on our GPU restricts the possible size of datasets, so we decompose CT images into overlapping sub-volumes, which are processed sequentially, with each sub-volume benefiting from the CUDA based parallelization.

Table 2.1: Filter taps for optimal differentiators of first (d_1) and second order (d_2) with 5 taps and their corresponding prefilters (p). Shown are half of the filter taps, the other half are determined by symmetry: the prefilter and even-order derivatives are symmetric and the odd-order derivatives anti-symmetric about the origin (sample number 0) [13]

	Sample Number		
	0	1	2
p	0.426375	0.249153	0.037659
d_1	0.000000	-0.276691	-0.109604
p	0.439911	0.249724	0.030320
d_2	-0.471147	0.002668	0.232905

For the calculation of the medialness, at each scale σ we compute the eigen-values $|e_1| \geq |e_2| \geq |e_3|$ and the associated eigenvectors $\mathbf{v}_1$, $\mathbf{v}_2$ and $\mathbf{v}_3$ of the Hessian matrix $\mathcal{H}^\sigma(\mathbf{x})$:

$$\mathcal{H}^{\sigma_i}(\mathbf{x}) = \begin{bmatrix} I^\sigma_{xx}(\mathbf{x}) & I^\sigma_{xy}(\mathbf{x}) & I^\sigma_{xz}(\mathbf{x}) \\ I^\sigma_{yx}(\mathbf{x}) & I^\sigma_{yy}(\mathbf{x}) & I^\sigma_{yz}(\mathbf{x}) \\ I^\sigma_{zx}(\mathbf{x}) & I^\sigma_{zy}(\mathbf{x}) & I^\sigma_{zz}(\mathbf{x}) \end{bmatrix}$$

where $I^\sigma(\mathbf{x}) = G_\sigma \star I_c(\mathbf{x})$ is the CT image convolved with a Gaussian kernel with variance σ and $I^\sigma_{xx}(\mathbf{x})$ is the second derivative in x-direction computed with the optimal filter tabs from [13], Table 2.1 (analogue $I^\sigma_{yy}(\mathbf{x})$, $I^\sigma_{zz}(\mathbf{x})$, $I^\sigma_{xy}(\mathbf{x})$, $I^\sigma_{zy}(\mathbf{x})$ and $I^\sigma_{xz}(\mathbf{x})$). The eigenvector $\mathbf{v}_3$ represents the tangent direction of the vessel segment, $\mathbf{v}_1$ and $\mathbf{v}_2$ span a cross section plane as illustrated in Figure 2.8.

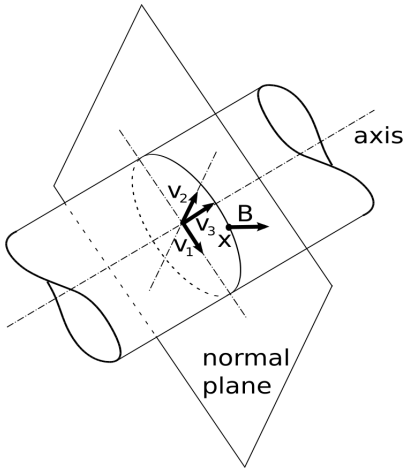

Figure 2.8: Based on the eigenvectors $\mathbf{v}_1$, $\mathbf{v}_2$ and $\mathbf{v}_3$ of the Hessian matrix the tubes cross section plane orientation is estimated and gradient information $\mathbf{B}$ at surface points x along a circle in this plane contribute to the offset medialness computation [4].

We define the boundary gradient

$$\mathbf{B}(\mathbf{x}, \sigma) = \sigma \nabla I^\sigma(\mathbf{x})$$

An initial response is given by the median of the boundary contributions

$$b_{i,\sigma} = |\mathbf{B}(\mathbf{x} + r\mathbf{v}_{\alpha_i}, \sigma)\mathbf{v}_{\alpha_i}|$$

with $i = 1 \ldots \lfloor 2\pi r + 1 \rfloor$ and r being the radius varying from 1.0 to 2.0, $\Delta_r = 0.3$, which we denote as R_0^+. A problem of $R_0^+(\mathbf{x}, r, \sigma)$ is, that it also produces responses at isolated

edges. To avoid this, a measure of symmetry is introduced:

$$S(\mathbf{x}, r) = 1 - \frac{s(\mathbf{x}, r)}{\bar{b}}$$

where $s(\mathbf{x}, r)$ is the median absolute deviation of the boundary samples and $\bar{b}$ is its median. The final boundary response is computed as:

$$R^{+}(\mathbf{x}, r, \sigma) = R_0^{+}(\mathbf{x}, r, \sigma) S(\mathbf{x}, r)^{\frac{3}{2}}$$

To suppress responses at the border of vessels, the gradient magnitude at the center of the vessel is used:

$$R^{-}(\mathbf{x}, r, \sigma) = \sigma_i |\nabla I^{\sigma_i}(\mathbf{x})|$$

$R^{-}(\mathbf{x}, r, \sigma)$ is combined with the offset medialness from above, such that the boundary measure is only used, if it is larger than the gradient at the center of the circle with radius r.

$$R(\mathbf{x}, r, \sigma) = \max\{R^{+}(\mathbf{x}, r, \sigma) - R^{-}(\mathbf{x}, r, \sigma), 0\}$$

The final vesselness response

$$R_{multi}(\mathbf{x}) = \max_{\sigma, r} \{R(\mathbf{x}, r, \sigma)\}$$

is the maximum response from all different scales σ and radii r. We found 4 scales and radii r varying from 1 to 2 pixels, with an increase of 0.3 pixels to have the best performance.

Figure 2.9a shows an example of the vessel filter response, where locations with high vessel probability are shown in red.

2.3.5 Non-maxima Suppression

In a non-maxima suppression step inspired by [4], at each position $\mathbf{x}$ with a medialness $R(\mathbf{x}) > th_{min}$, we sample 8 points on the unit circle on a plane perpendicular to the estimated vessel direction. If the medialness on any of these 8 points is larger than at the current position $\mathbf{x}$, $R(\mathbf{x})$ is set to zero. This leads to disconnected vessel centerline fragments due to branching points of the vessels, where the tubular model assumption fails. Figure 2.9b depicts the non-maxima suppressed centerline fragments in green.

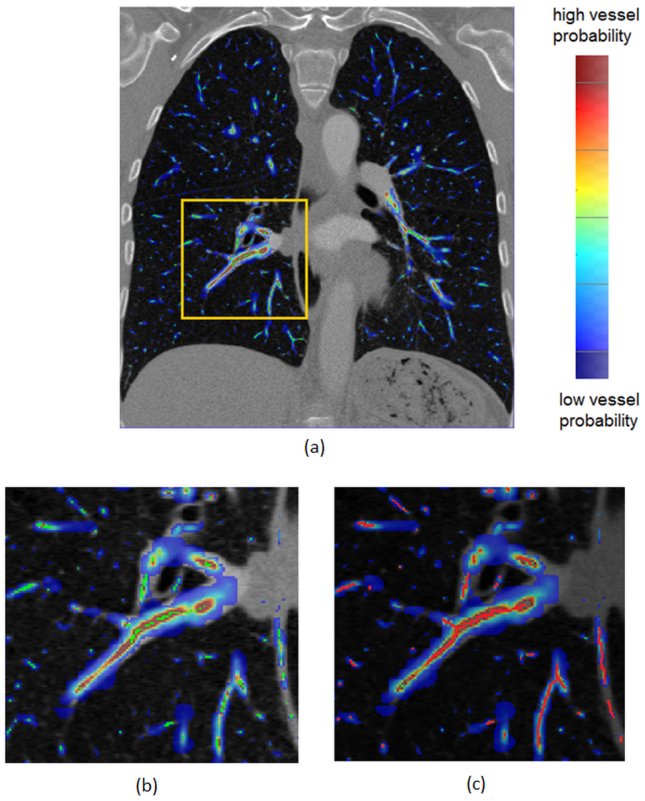

Figure 2.9: Vessel enhancement filter response in the lung vessels (a), non-maxima suppressed response (b, green lines), connected centerline (c, red lines)

2.3.6 Centerline Reconnection

For vessel structure analysis it is important to have a fully connected vessel tree. However, the vessel enhancement filter has problems in branching regions of vessels, because the tubular model assumption is not fulfilled. This leads to disconnected centerline fragments after non-maxima suppression. We propose an efficient shortest path algorithm that takes a combination of different information into account, to produce a single connected vessel centerline tree.

As a preprocessing step, small centerline fragments (less than 5 N_{26}-connected voxels) are removed and all maxima lying on the airway border are cleared using the airway segmentation from Section 2.1. For the reconnection of the vessel centerlines, we apply a modified version of the graph search approach presented in the intelligent scissors algorithm [43]. Starting from one root point p_r in the CT image, the costs and the cheapest path from all voxels to p_r are computed. We use three data structures, a sorted stack S_A holding voxel coordinates and the corresponding costs, a volume I_{cum} having the same

size as the CT image that will hold the cumulative costs, and a volume I_{ptr} with the same size as the CT image for storing pointers for the cheapest path. The stack S_A is sorted such that voxels with the smallest costs are on top. As initialization, we set all voxels in I_{cum} to infinity, except the root p_r which has zero cost and we push the root point p_r onto the stack. The algorithm works as follows: As long as the stack S_A is not empty, take the position p with the lowest cost off the stack and for each N_{26}-connected neighbour $n(p)$, compute the cost

$$c_i = I_{cum}(p) + I_c(n(p))$$

where i is the neighbour index. If c_i is lower than $I_{cum}(n(p))$, then save the new cost in I_{cum}, push the neighbour $n(p)$ onto the stack and save a pointer from the neighbour $n(p)$ to p in I_{ptr}.

Since all vessels are connected to the heart we choose the center of the heart as root p_r. In our datasets we found that the center of the image is a good approximation of the heart. The cost map includes information from the normalized medialness R, the maxima of the medialness R_{maxima}, and the normalized image gradient magnitude $|\nabla I|$:

$$I_c = \left(\sqrt[3]{|\nabla I|} + e^{-10R} \right) (1 - R_{maxima})$$

The cube root from the gradient magnitude image was computed to give higher cost to small edges and the scaling factor of 10 for the medialness was found empirically. To avoid wrong connections through the mediastinum, we process each lung separately. The connected trees of the right and left lung form the final vessel tree.

2.3.7 Graph Generation

For a later analysis of the vascular structure, a higher level representation of the vessel centerlines is needed. We construct a graph with vessel branching points as vertices and the vessels as the edges between the branching points. We start with classifying the centerline voxels as branching points (more than 2 neighbouring centerline voxels in a twenty-six neighbourhood) or edge points (exactly two neighbours). As root for the graph the same voxel as for the centerline reconnection is taken. Using a recursive algorithm, the graph is generated until all centerline voxels have been processed. Figure 2.10 shows an example of a graph generated from the connected vessel centerlines. Green boxes represent endpoints and branching points, the edges (vessel segments) are plotted with different colours.

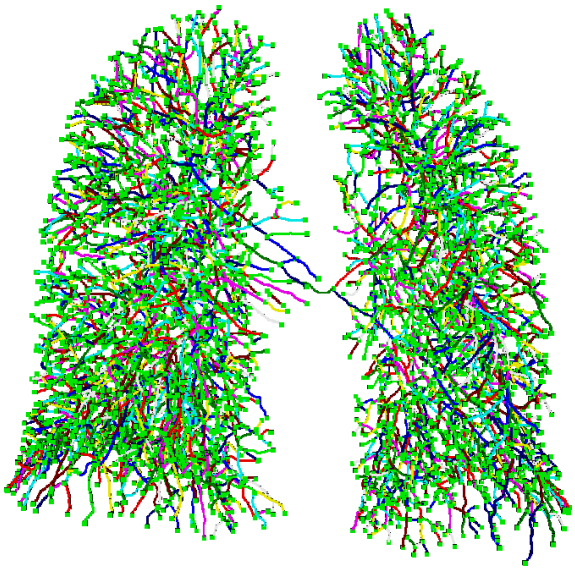

Figure 2.10: 3D rendering of the graph representing the vascular tree

2.3.8 Vessel Radius Estimation

The vessel segmentation consists of two steps: first a coarse radius detection is performed using the vessel centerlines as input, then a geodesic active contour algorithm [50] is applied for the final segmentation, thus enabling the segmentation to snap onto the image gradients.

For the coarse detection of the vessel radius we use the centerlines as initialization. At each vessel centerline point, we sample points lying on a sphere from the CT-image and accumulate the grey values. This is done for different sphere radii $r_s = 0.1 \ldots 15\,\text{mm}$, increment $\Delta = 0.1\,\text{mm}$. Figure 2.11 shows the normalized sum of grey values for 4 different positions at different vessels. The advantage of using a sphere instead of a plane perpendicular to the estimated vessel direction is, that it is more robust and does not need the vessel direction estimation. In branching points for example the vessel direction cannot be estimated correctly, which would then result in a wrong radius estimation. This coarse segmentation is used as initialisation for a geodesic active contour model. In Figure 2.12 an example vessel segmentation is illustrated.

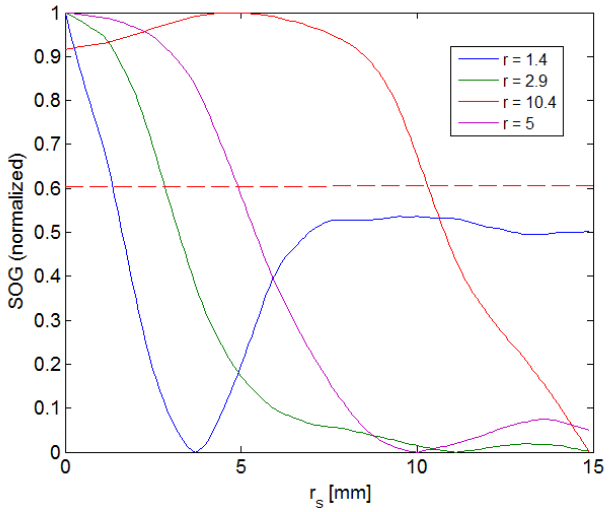

Figure 2.11: Examples for the sum of grey values (SOG) of points sampled on a sphere with different radii r_s. The intersection with the empirically found value of 0.6 indicates the vessel radius.

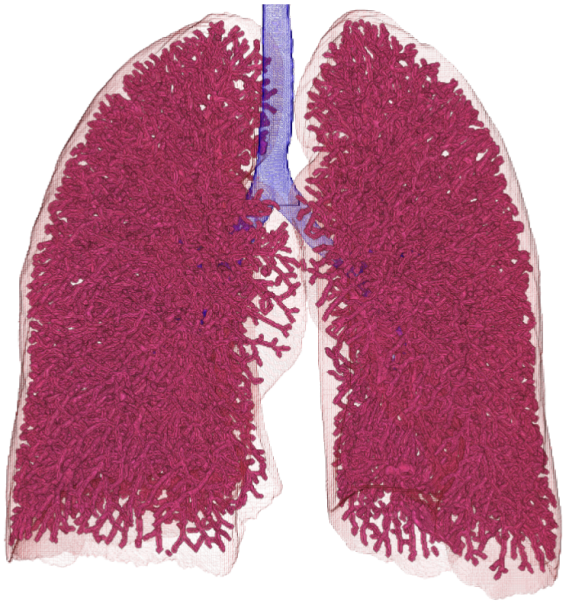

Figure 2.12: 3D Rendering of a vessel segmentation

Chapter 3

Experiments and Results

Contents

In this section results from our algorithm are presented. First we show segmentations of a phantom liver vessel tree, where we successively add Gaussian noise to test the robustness of our algorithm. Then we apply the algorithm to the publicly available VESSEL12 challenge dataset. As third dataset we use 24 CT scans from patients who underwent contrast enhanced CT as a part of a clinical PH study at the Ludwig Boltzmann Institute for Lung Vascular Research, Graz (see Appendix C for detailed information about the patients included in the study). From the 24 patients we show the results of the airway- and lung-segmentation and the reconstructed vascular trees.

3.1 Implementation Details

All of our filters are implemented in CUDA, which is a parallel programming model from NVIDIA, that generates hardware accelerated instructions for NVIDIA graphics processing units (GPUs). Using CUDA we can significantly improve the runtime of our 3D image processing algorithms due to the high degree of parallelization. Limited memory on our GPU restricts the possible size of datasets, therefore we decompose CT images into overlapping sub-volumes, which are processed sequentially, with each sub-volume benefiting

from the CUDA based parallelization. To further decrease the computation time and memory requirements, we crop the CT images according to the bounding extents of the lung mask after lung segmentation and perform all further computations on the cropped CT scan. This way, we can directly work on the full resolution CT data. The runtime of the CUDA implementation of the whole algorithm pipeline ranges from 5 to 10 minutes, whereas a CPU-only implementation would need more than an hour.

3.2 Phantom Data

We used a phantom of a liver vessel tree, shown in Figure 3.2a, to check the performance of the algorithm and validate its robustness against noise. We successively added Gaussian noise with increasing variance to the phantom data (Figure 3.1) and calculated the Jaccard index of the ground-truth segmentation with the obtained segmentation. The curve in Figure 3.2b shows how the Jaccard index changes if Gaussian noise with increasing variance is added to the phantom dataset. As long as the variance of the noise is below 40 Hounsfield Units (HU), the performance lies above 93% segmentation overlap.

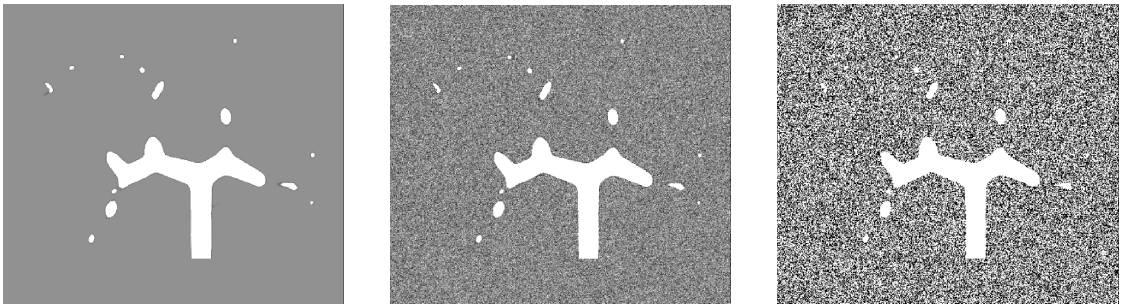

(a) $\sigma = 0$ (b) $\sigma = 20$ (c) $\sigma = 80$

Figure 3.1: Coronal slice of the liver vessel phantom with increasing Gaussian noise. For visualization purposes the window level for all three images has been modified.

3.3 VESSEL12 Challenge Dataset

To be able to compare our algorithm to other approaches, we tested it on 20 CT scans which were provided by the organizers of the *VESSEL12 Challenge* workshop. For information about obtaining the reference segmentations and the exact definition of the used performance measures we refer to the official website*. The generated segmentations were

*http://vessel12.grand-challenge.org/

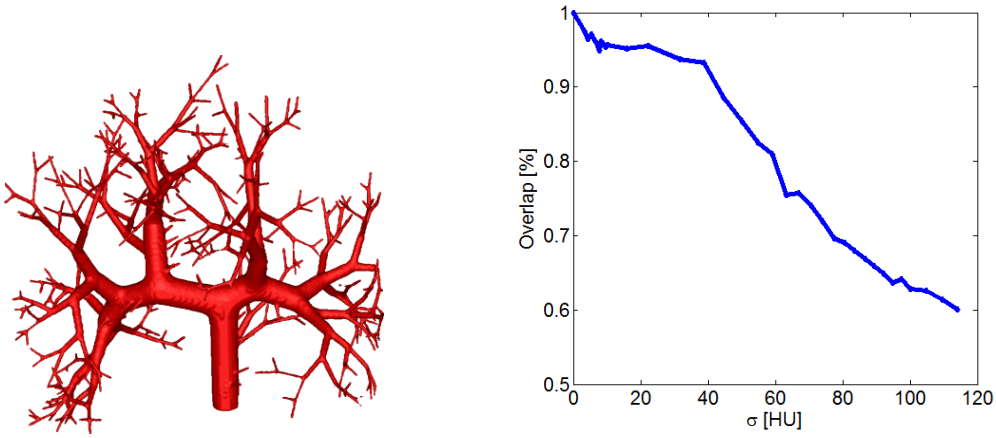

(a) (b)

Figure 3.2: (a) 3D rendering of liver vessel phantom, (b) Jaccard index over variance of Gaussian noise

sent to the organizers, who in return provided evaluation results. Table 3.1 summarizes the evaluation results for the 20 testing datasets. On average, our algorithm achieved a specificity of 0.971 and a sensitivity of 0.742. The area under the curve was $A_z = 0.863$. We performed very well in terms of specificity, however improvement in the sensitivity is still necessary. With these results, we occupy a midfield position among all participating teams. Reasons for this performance of the algorithm is the optimization for the contrast-enhanced setup and the use of isotropic CT scans which is not the case in all VESSEL12 datasets. We see room for improvement for detecting small vessels, smaller than $2-3\,\text{mm}$ in diameter, which are misclassified as noise and hence not included in the segmentations. All results from the other participating groups can be found on the official VESSEL12 challenge website.

3.4 PH Study Dataset

As a third dataset, we use 24 contrast enhanced CT scans, with a median size of $512 \times 512 \times 426$ pixel, from patients who took part in clinical PH study conducted by the Ludwig Boltzmann Institute for Lung Vascular Research, Graz (LBI-LVR). In Appendix C detailed information about the clinical data from the patients can be found. We do not have any ground truth information on the vessels, however together with the experts from the LBI-LVR, we quantitatively evaluated the segmentations and found them suitable

Table 3.1: Evaluation results from the VESSEL12 challenge in comparison with the best team (Anon_feat_learning)

	Our Team			Anon_feat_learning		
	Az	**Specificity**	**Sensitivity**	**Az**	**Specificity**	**Sensitivity**
All Vessels/Non-vessels	0.863	0.971	0.742	0.986	0.941	0.949
VESSEL12_01	0.742	0.997	0.485	0.993	0.931	0.978
VESSEL12_02	0.938	0.965	0.889	0.988	0.936	0.944
VESSEL12_03	0.956	0.973	0.923	0.994	0.950	0.978
VESSEL12_04	0.822	0.953	0.672	0.981	0.926	0.916
VESSEL12_05	0.97	0.96	0.953	0.987	0.912	0.991
VESSEL12_06	0.795	0.988	0.602	0.976	0.886	0.969
VESSEL12_07	0.899	0.973	0.81	0.993	0.916	0.990
VESSEL12_08	0.943	0.955	0.906	0.978	0.936	0.918
VESSEL12_09	0.896	0.973	0.806	0.985	0.956	0.949
VESSEL12_10	0.835	0.989	0.678	0.988	0.982	0.901
VESSEL12_11	0.81	0.996	0.625	0.992	0.984	0.931
VESSEL12_12	0.778	0.994	0.561	0.984	0.978	0.924
VESSEL12_13	0.796	0.981	0.605	0.994	0.972	0.904
VESSEL12_14	0.861	0.949	0.755	0.978	0.901	0.968
VESSEL12_15	0.917	1	0.833	0.993	0.973	0.956
VESSEL12_16	0.89	0.982	0.786	0.993	0.978	0.951
VESSEL12_17	0.937	0.96	0.897	0.982	0.909	0.983
VESSEL12_18	0.926	0.942	0.876	0.988	0.909	0.969
VESSEL12_19	0.892	0.983	0.793	0.996	0.986	0.938
VESSEL12_20	0.882	0.925	0.795	0.990	0.898	0.976
Small vessels/Non-vessels	0.781	0.971	0.585	0.977	0.932	0.932
Medium vessels/Non-vessels	0.848	0.971	0.716	0.986	0.953	0.949
Large vessels/Non-vessels	0.951	0.971	0.909	0.994	0.961	0.961
Vessels/Airway walls	0.851	0.928	0.742	0.944	0.745	0.949
Vessels/Dense abnormalities	0.712	0.572	0.742	0.667	0.291	0.949
Vessels/Mucus-filled bronchi	0.677	0.439	0.742	0.595	0.133	0.949
Vessels in dense abnormality/Dense abnormalities (Contrast scans only)	0.646	0.663	0.582	0.654	0.478	0.795
Vessels/Nodules (CAD)	0.659	0.46	0.742	0.439	0.072	0.949

for further analysis. In the subsequent sections we show the results of the airway- and lung-segmentation and the reconstructed vascular trees from these 24 patients.

3.4.1 Airway Segmentations

In this section we present segmentations of the airway tree from patients included in the PH study. One segmentation took on average 68 seconds. Table 3.2 gives a quantitative overview of the airway segmentation results, in Figure 3.3 and Figure 3.4 3D renderings of segmentations of the airways are shown.

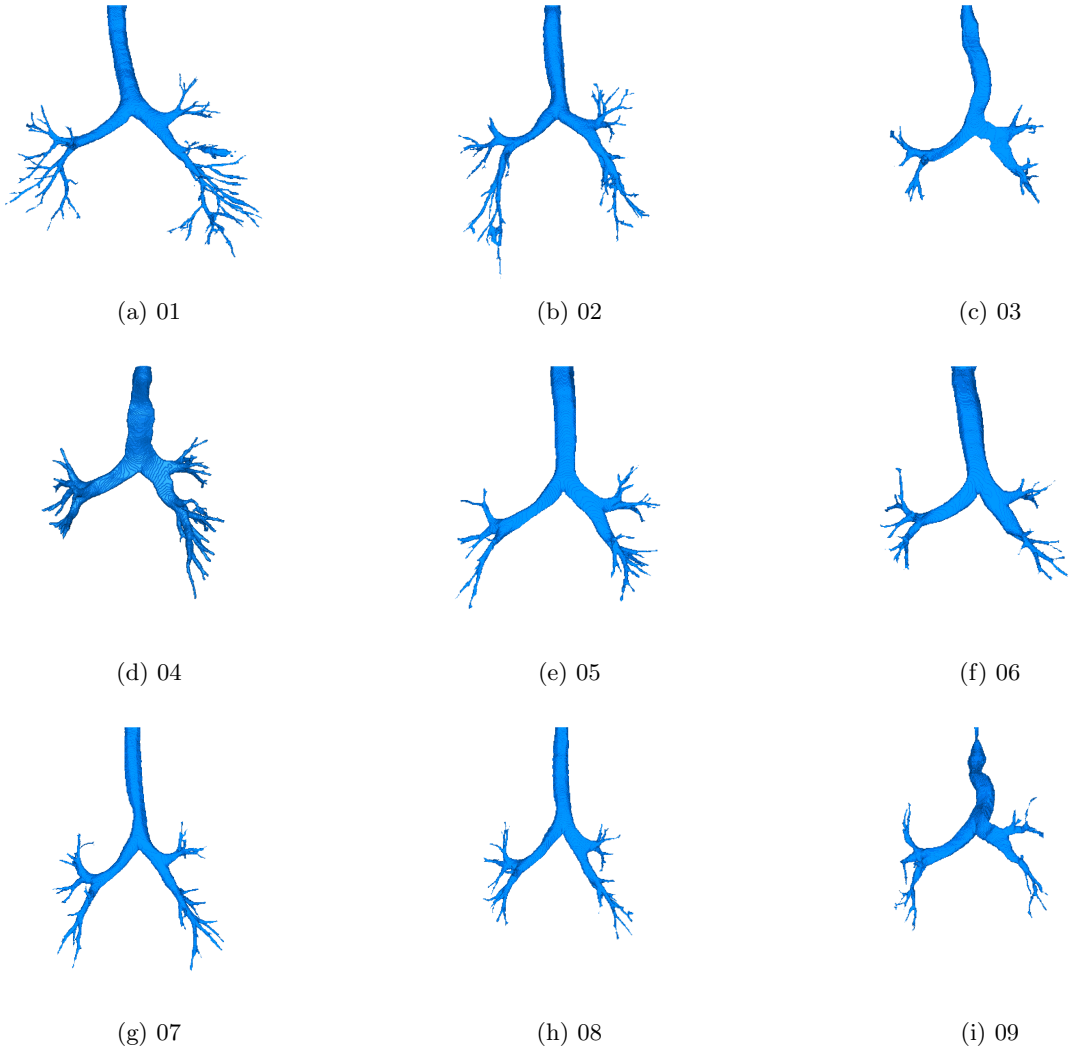

(a) 01 (b) 02 (c) 03

(d) 04 (e) 05 (f) 06

(g) 07 (h) 08 (i) 09

Figure 3.3: Airway segmentations from patients of the clinical PH study. The sub figure captions indicate the patient number.

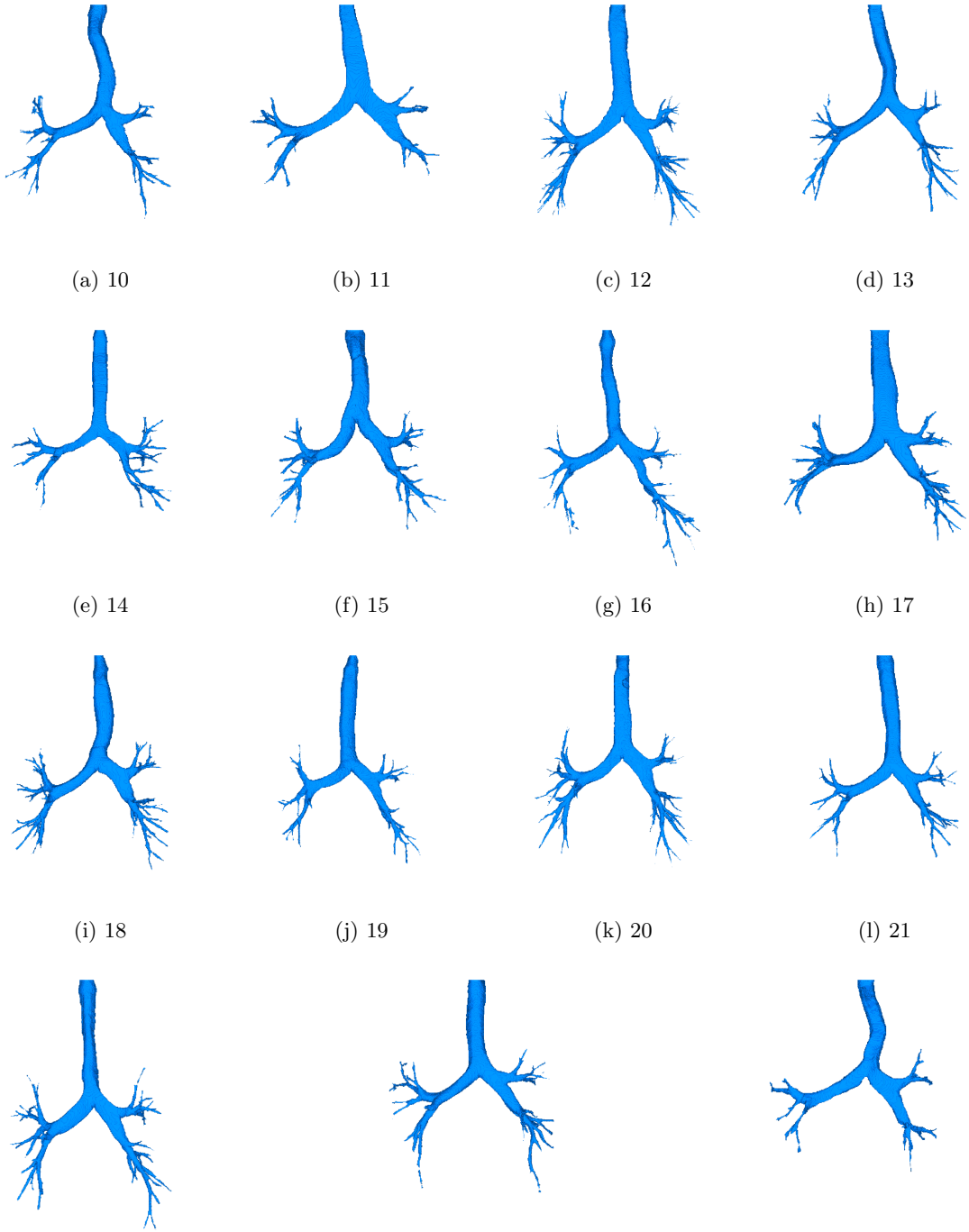

(a) 10 (b) 11 (c) 12 (d) 13

(e) 14 (f) 15 (g) 16 (h) 17

(i) 18 (j) 19 (k) 20 (l) 21

(m) 22 (n) 23 (o) 24

Figure 3.4: Airway segmentations from patients of the clinical PH study. The sub figure captions indicate the patient number.

Table 3.2: The obtained airway characteristics from patients of our PH study

Patient number	**Number of branches**	**Volume [ml]**	**Segmentation time [s]**
01	200	45	96
02	162	41	65
03	60	29	57
04	111	52	83
05	82	44	64
06	79	50	71
07	106	39	62
08	88	30	59
09	56	30	60
10	91	44	70
11	54	35	67
12	166	78	57
13	86	40	78
14	77	25	68
15	100	53	48
16	89	30	52
17	111	70	82
18	124	43	69
19	78	45	52
20	136	72	76
21	84	52	81
22	108	76	80
23	78	48	70
24	45	21	87
mean ± SD (range)	98.792 ± 37.368 (45-200)	45.2 ± 15.72 (21-78)	68 ± 12 (48-96)

3.4.2 Lung Segmentations

Figure 3.5 and Figure 3.6 show lung segmentations in difficult cases (patients having e.g. scleroderma), and simpler cases, respectively. To be able to properly segment the lung of all patients, more prior knowledge about the lung needs to be utilized (using for example a generative model of shape and/or appearance, or using the rib cage as reference [56]). In Table 3.3 the volumes of the segmented lungs for each patient are listed.

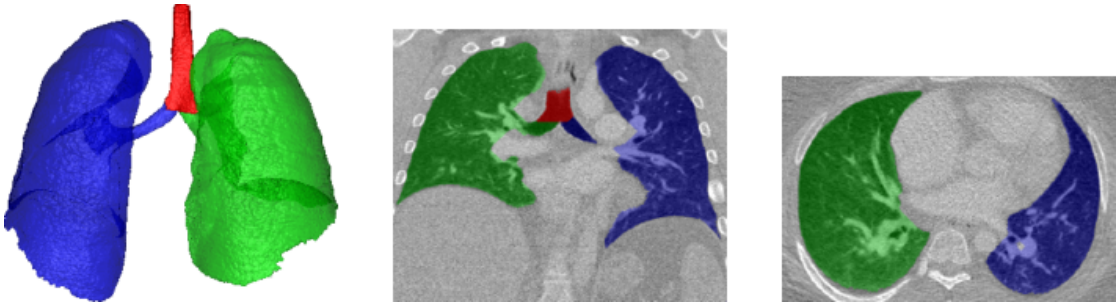

(a) 11

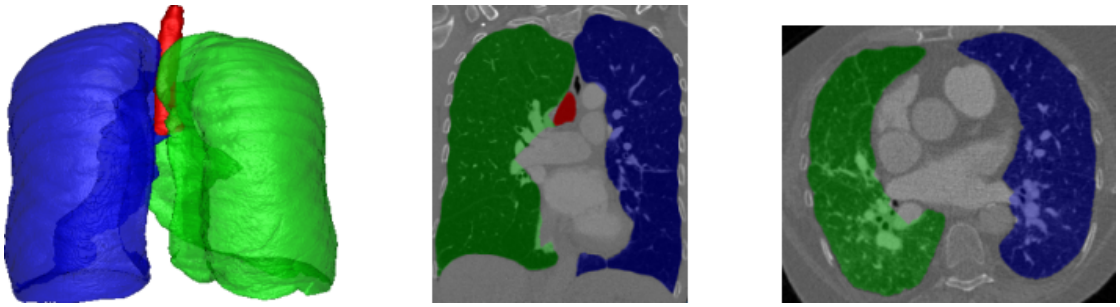

(b) 19

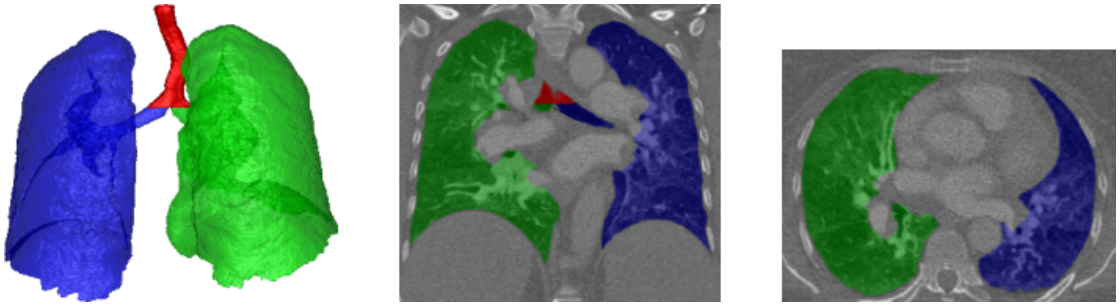

(c) 24

Figure 3.5: Difficult cases for the lung segmentation (patients with severe lung pathologies and/or hardly visible fissures between left and right lung). The first column shows 3D renderings of lung segmentations, coronal and axial views are depicted in column two and three, respectively. The sub figure captions indicate the patient numbers.

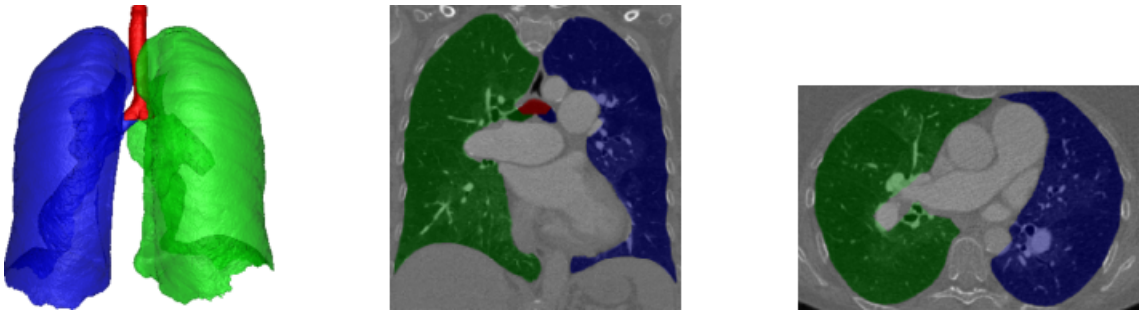

(a) 02

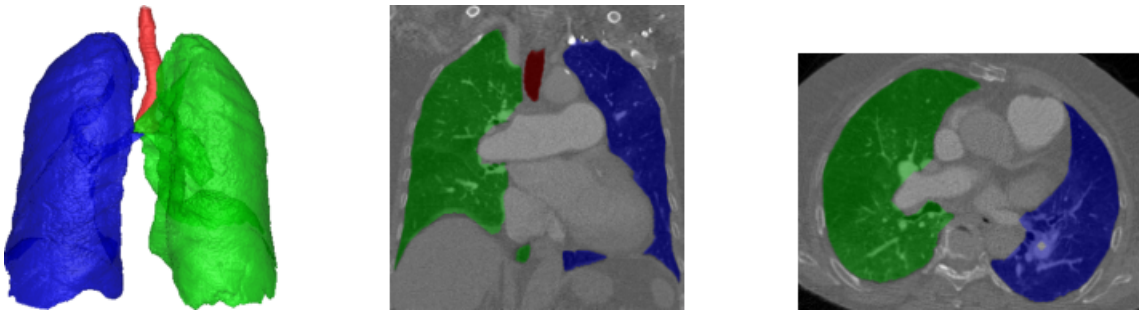

(b) 03

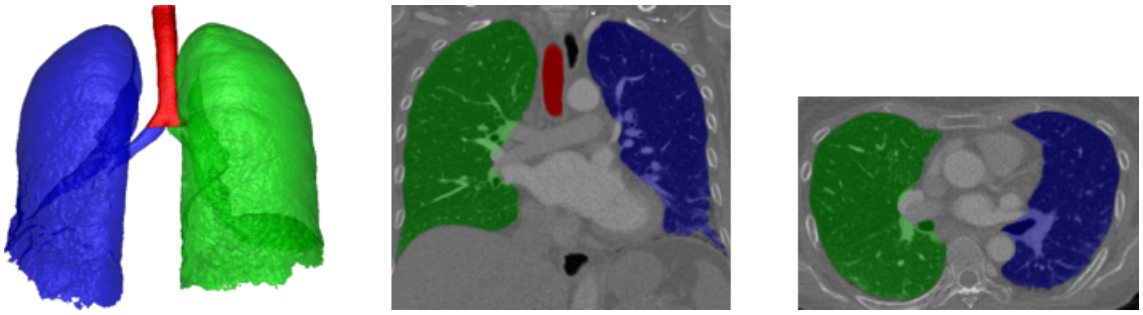

(c) 05

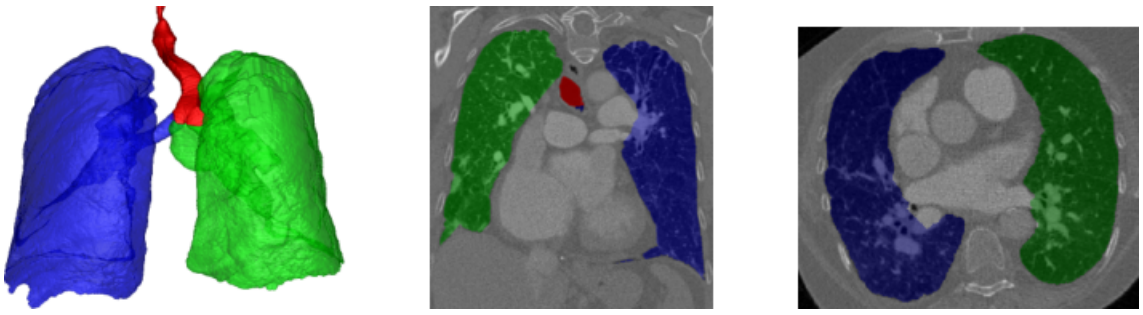

(d) 09

Figure 3.6: Lung segmentations of patients not showing severe diseases affecting the lung parenchyma. The first column shows 3D renderings of lung segmentations, coronal and axial views are depicted in column two and three, respectively. The sub figure captions indicate the patient numbers.

3.4.3 Pulmonary Vascular Trees

Figure 3.7, Figure 3.8 and Figure 3.9 are showing 3D renderings of the lung segmentations (brown), the airway segmentations (blue) and the extracted vessel centerlines (red) from patients of the clinical PH study. In Table 3.3 the number of detected vessel segments for each patient is listed.

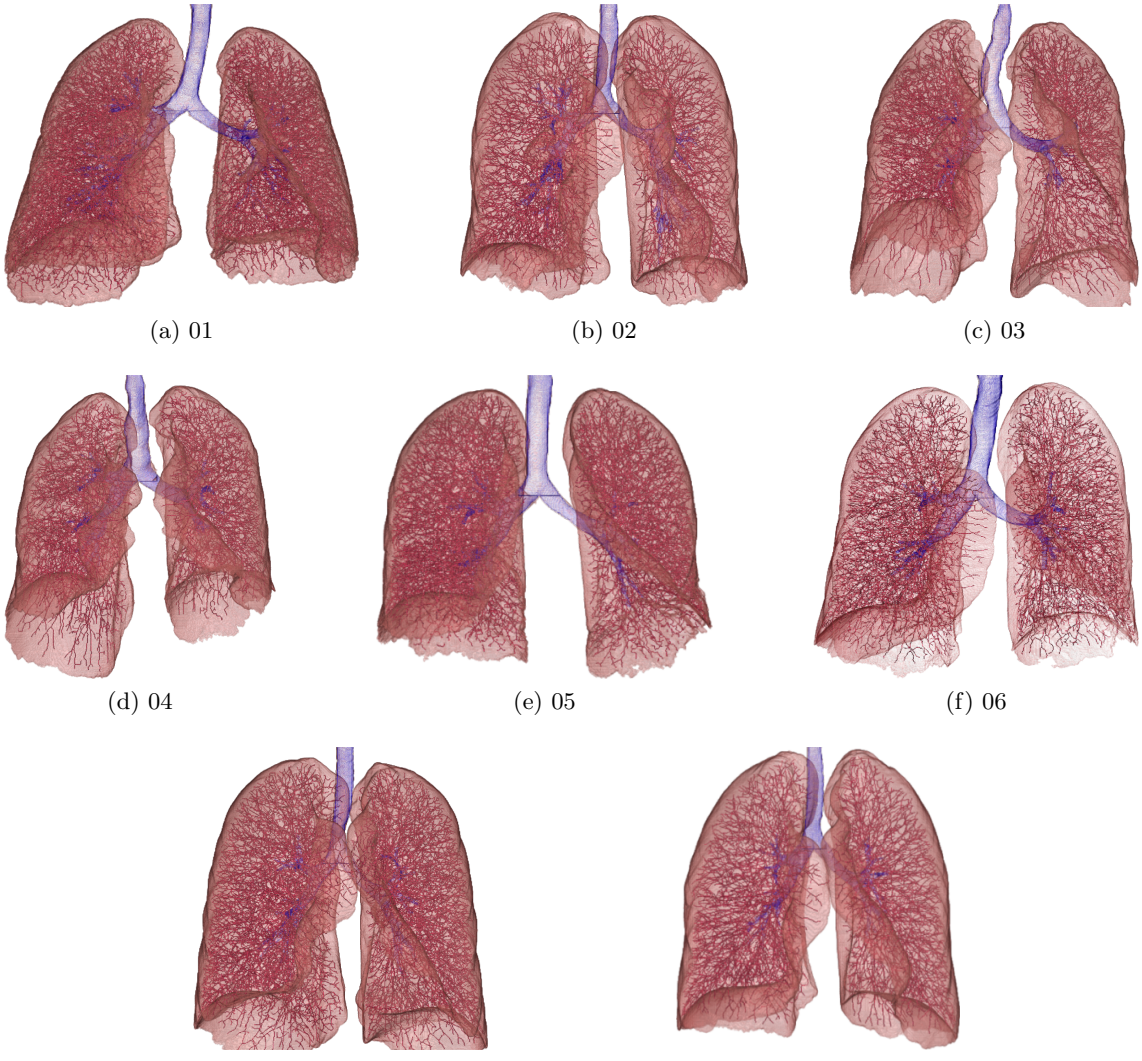

(a) 01 (b) 02 (c) 03

(d) 04 (e) 05 (f) 06

(g) 07 (h) 08

Figure 3.7: 3D renderings of the lungs, airways and the vessel centerlines. The sub figure captions indicate the patient number.

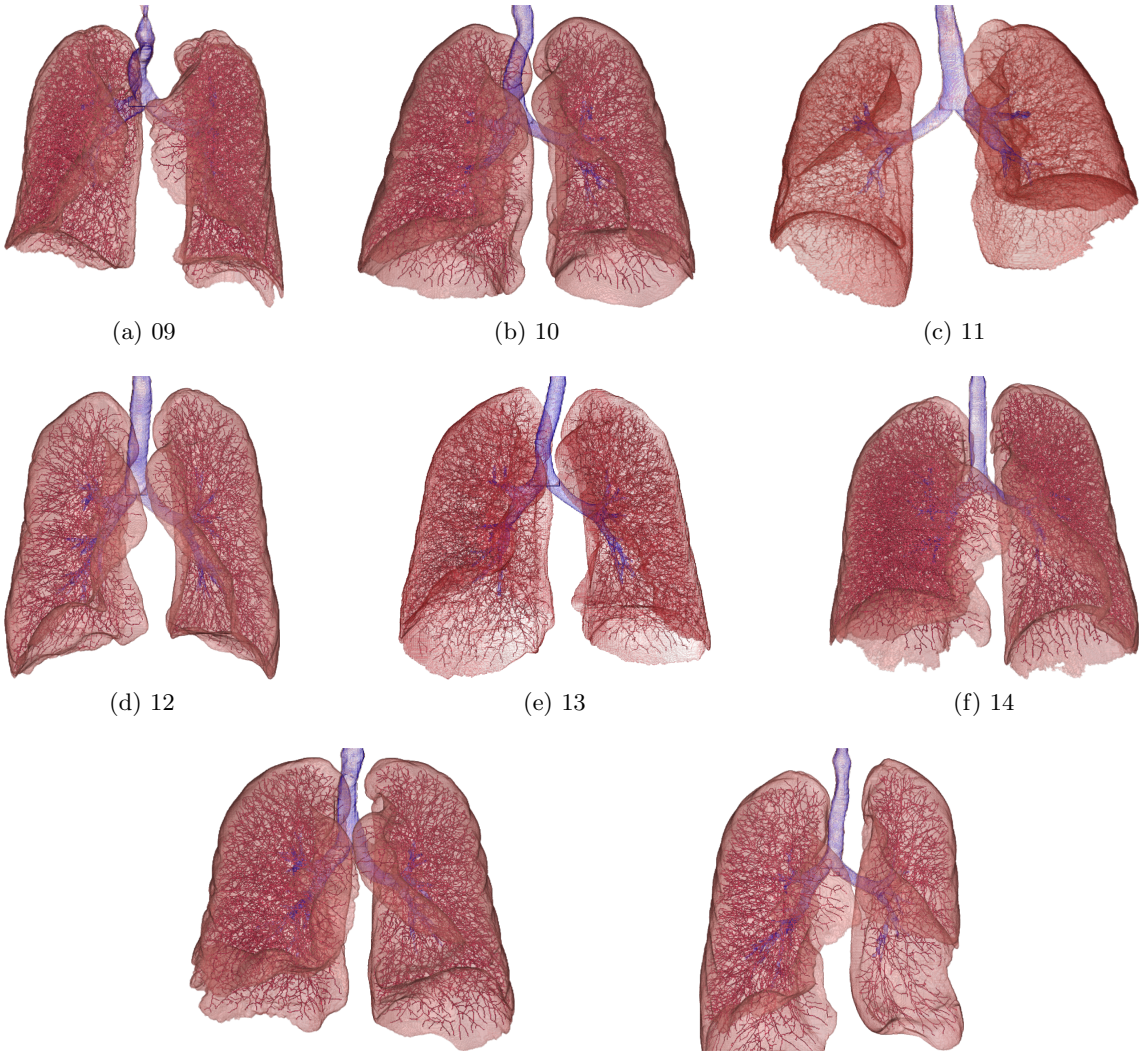

(a) 09 (b) 10 (c) 11

(d) 12 (e) 13 (f) 14

(g) 15 (h) 16

Figure 3.8: 3D renderings of the lungs, airways and the vessel centerlines. The sub figure captions indicate the patient number.

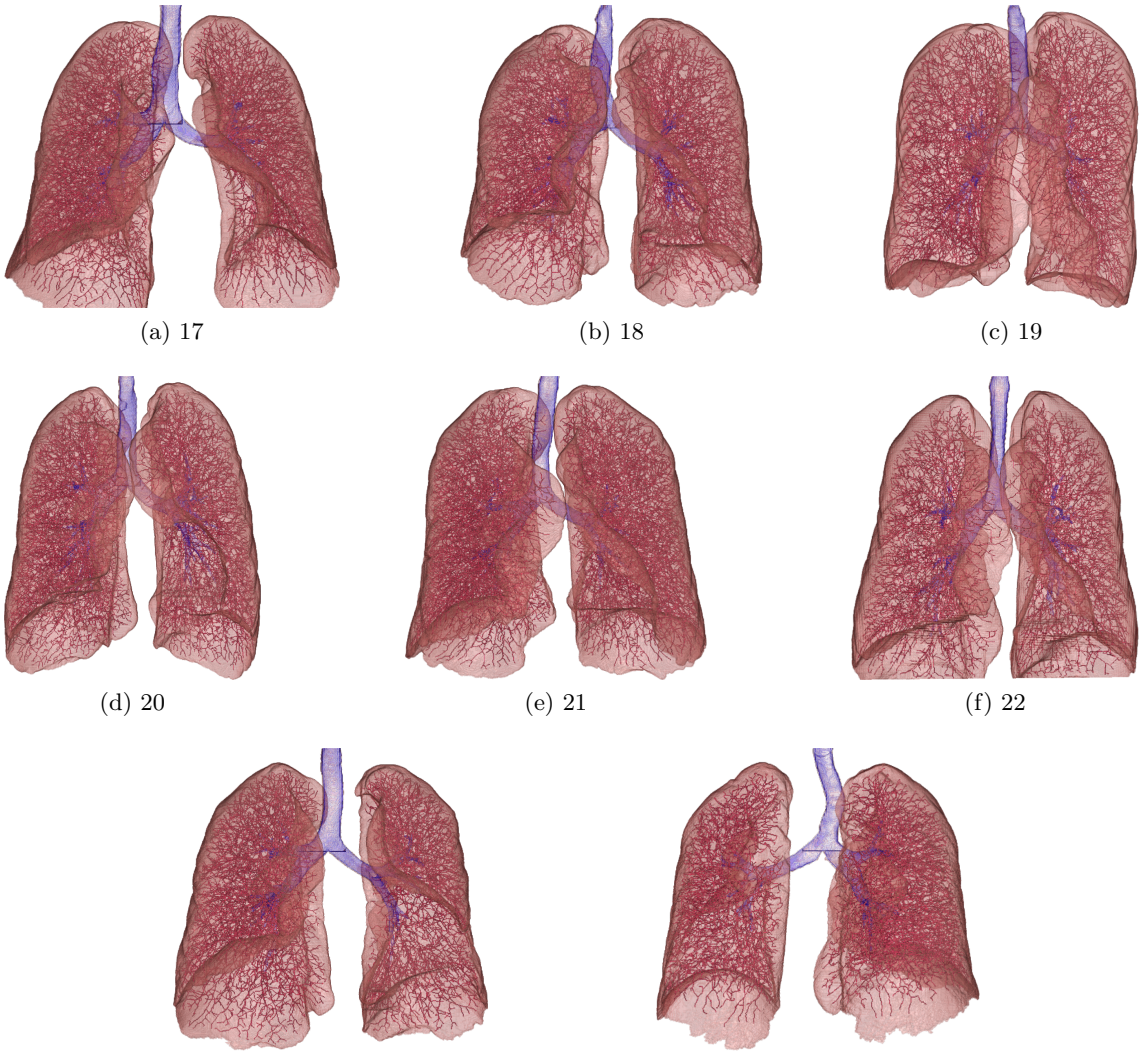

(a) 17 (b) 18 (c) 19

(d) 20 (e) 21 (f) 22

(g) 23 (h) 24

Figure 3.9: 3D renderings of the lungs, airways and the vessel centerlines. The sub figure captions indicate the patient number.

Table 3.3: Number of vessel segments and lung volumes from patients in the PH study

Patient number	**Lung volume [ml]**	**Number of vessel segments [10^{-3}]**
01	4108	16.628
02	3890	7.955
03	3066	8.391
04	4159	11.988
05	2934	12.804
06	3682	11.418
07	5373	13.335
08	4582	14.642
09	2632	15.179
10	5958	12.196
11	2804	12.441
12	5924	8.838
13	5122	16.609
14	3362	18.056
15	5144	11.241
16	3182	7.815
17	4460	12.181
18	4808	12.230
19	5707	10.873
20	6487	20.434
21	5448	17.292
22	6621	11.179
23	3679	10.960
24	1973	10.059
mean ± SD	4379 ± 1294	12.233 ± 3.575
(range)	(1973-6621)	(7.815-20.434)

3.5 Discussion of the Results

We showed that the algorithm works well on the data sets from our PH patient cohort, consisting only of isotropic contrast-enhanced scans. We found the detected centerlines to be correct in almost all cases, which is a crucial requirement for the later analysis. Also the experts from the Ludwig Boltzmann Institute for Lung Vascular Research found the centerlines suitable for further analysis. However, in case of the VESSEL12 challenge, where we occupy a midfield position among all participating teams, the vessel enhancement filter is not sensitive enough to small vessels which have a very low contrast. Reasons are that our image filters do not yet take the anisotropy of the VESSEL12 data sets into account, and our algorithm is optimized for the contrast enhanced setup.

Chapter 4

Analysis of the Vessel Tree

Contents

Vascular morphology has been used as diagnostic parameter and to quantify disease severity in several studies. The works in [15] and [16], for example, attempt to quantitate carotid stenosis by analysis of vessel morphology. Bullit et al. [8] distinguishes malignant from benign brain tumors by calculating the tortuosity of the vessels. In another work, Gerig et al. [19] aims to characterize aortic aneurysms using the topology of vessels in the brain. In this chapter we will investigate two readouts to describe the lung vessel structure and complexity. We will also correlate the calculated measures with actual clinical parameters derived from right heart catheterisation, and assess the usefulness of these parameters for pulmonary hypertension diagnosis and for monitoring disease progression.

4.1 Fractal Dimension

Images representing morphologically complex structures can be described using the fractal dimension (FD). The first object with fractal structure described in literature was the coast line of Britain [39]. From then on the FD was used for image analysis in the field of neuroscience, for complexity analysis of the vascular tree in the human retina [40], and for complexity analysis of the pulmonary vessel tree [21]. Haitao et al. [23] and Moledina et al. [42] showed that pulmonary hypertension is correlated with the two dimensional fractal dimension of the pulmonary vessel tree. However, their results are contradictory.

These two papers inspired us to extend the fractal dimension into three dimensions and apply it for vascular analysis.

4.1.1 Theory

In the 1960s Benoit Mandelbrot introduced the term "fractal" to better measure rough shapes and irregular surfaces, from graphs of the stock market to coastlines. The most important property of a fractal is self-similarity [21]. An object is self-similar if you can break the object down into an arbitrary number of smaller pieces and each of those pieces is a replica of the entire structure. The Sierpinski triangle in Figure 4.1 is a typical example for a fractal structure. The fractal dimension can be described theoretically by the Hausdorff dimension [12]. Given the fact that the Hausdorff dimension can not be directly assessed, an approximation is possible, using the concept of self-similarity. Consider an object consisting of distinct segments. If each segment is divided into r smaller segments, the resulting number N of smaller objects follows a power law:

$$N = r^{-FD} \tag{4.1}$$

Hence,

$$FD = -\frac{log\, N}{log\, r} \tag{4.2}$$

where FD is the dimension of the power law. For Euclidean objects, FD equals the Euclidean dimension (D=1,2,3,... n). Fractal objects obey a metric scaling relation, where the exponent is not equal to the Euclidean dimension and is usually non integer.

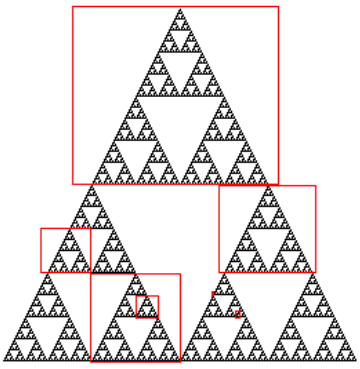

Figure 4.1: Sierpinski triangle, the small scale-form appears similar to its large-scale form

4.1.2 Box Counting

The 3D fractal dimension can be approximated by a 3D extension of the well-validated box counting method [41]. Box counting consists of dividing a binary image into a grid of boxes with equal size $\delta \times \delta \times \delta$ and counting the number of non-empty boxes N_δ containing part of the structure. This process is repeated for different box sizes (Figure 4.2). With increasing box size, the number of non-empty boxes exponentially decreases. The fractal dimension is equivalent to the slope of a line fitted to a double logarithmic plot of the number of non-empty boxes N_δ against the box size δ (Figure 4.3).

To reduce the influence of the discretization in the image, box counting is performed multiple times. In each iteration the starting position of the grid is shifted by an offset (0, 1, 2 and 3 pixels in each dimension). The FD is

$$FD = \frac{1}{N} \sum_{i=1}^{N} FD_i$$

where FD_i is the fractal dimension calculated at iteration i.

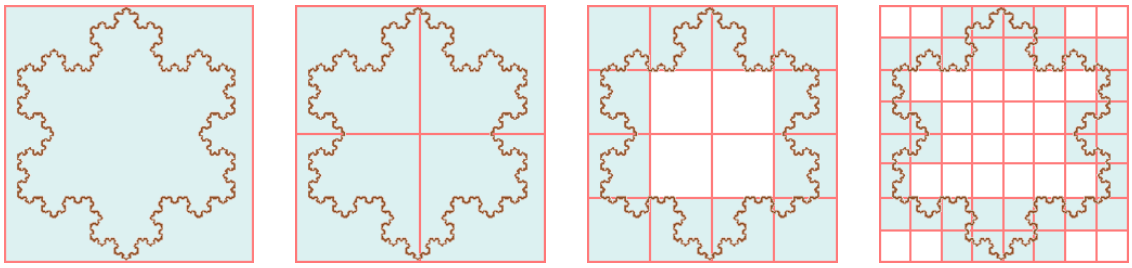

(a) (b) (c) (d)

Figure 4.2: Box counting method: the fractal structure is covered with boxes of varying size δ. The number of non-empty boxes N_δ (light blue) is counted. (a) number of boxes N = 1 (b) N = 4 (c) N = 16 (d) N = 64.

For estimation of the fractal dimension from the log-log plot, the slope of a fitted line has to be calculated. However, due to the limited CT resolution and the limited size, two effects have to be considered: finite N plateaus and staircasing/finite size plateaus (Figure 4.3). To account for limitations in resolution for line fitting, only the linear part was used (Figure 4.5b, red dots).

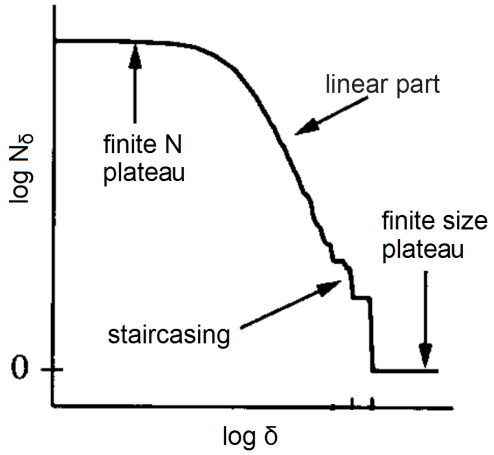

Figure 4.3: Real-world example of a log-log plot of the number of non-empty boxes N_δ against the box size δ. Because of a limited amount of data points N (limited resolution), a point is reached where one data point is covered with a single box. This leads to a *finite N plateau*. The other extreme is when boxes become bigger than the object and cover it completely. This leads to *finite size plateaus*. When the boxes are a little bit smaller than the object, *staircasing* is visible [32]. For a reasonable estimation of the fractal dimension, only the linear part of the curve should be considered.

4.1.3 Experiments and Results

First, we calculated the FD on two synthetic images, then we applied the box counting algorithm to the vessel centerlines of our patient cohort from the clinical PH study (n=24). For the clinical interpretation of the fractal dimension results see Section 5.

For validation of our box counting implementation, we created a 3D Sierpinski Triangle (3 iterations, FD = 2, Figure 4.4a) and a Menger Sponge (3 iterations, FD = 2.726, Figure 4.4c) using Wolfram Alpha*. The results show very good agreement with the theoretical FD values. For the Sierpinski Triangle our estimated FD was $FD_{est} = 1.9917$, and for the Menger Sponge it was $FD_{est} = 2.701$. The mean 3D fractal dimension from the pulmonary vessels of the patients from the PH study was FD = 2.35±0.06 (range: 2.21 - 2.44), see Table 4.1 for all values. The values are in good agreement with previously published FD of vessels in mice [34]. Figure 4.5a shows a 3D rendering of the vessel centerlines obtained from one patient. Figure 4.5b is the corresponding log-log plot from where the FD was estimated.

*www.wolframalpha.com

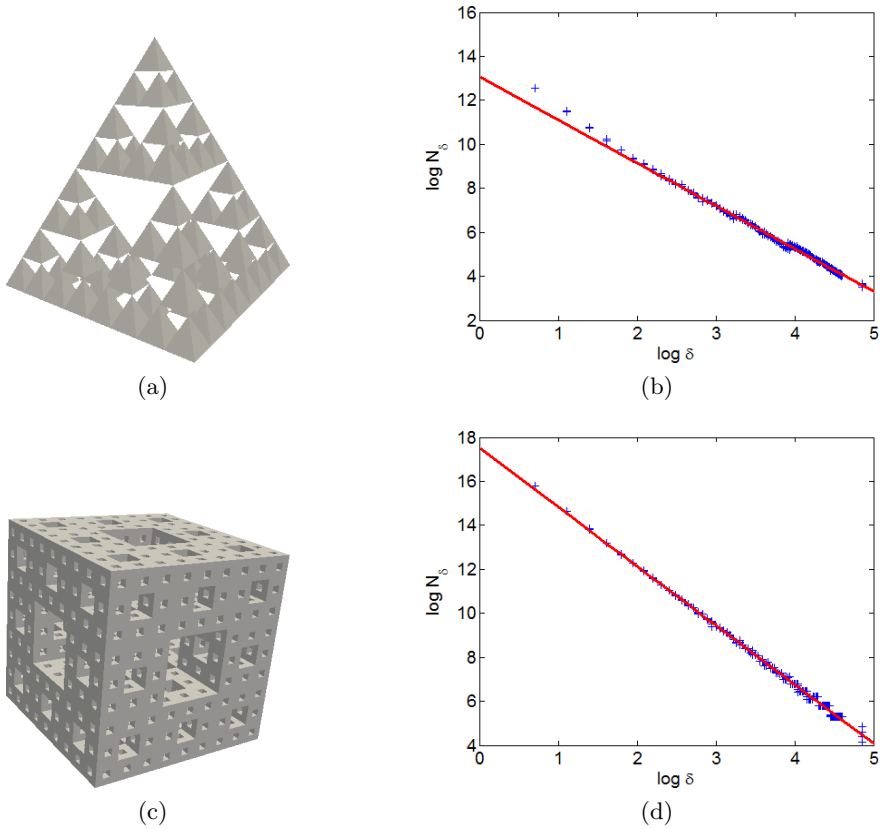

(a) (b) (c) (d)

Figure 4.4: (a) 3D Sierpinski gasket, $FD = 2$, (b) double logarithmic plot from the slope of the fitted red line corresponds to $FD_{est} = 1.9917$, (c) 3D Menger Sponge, $FD = 2.726$, (d) double logarithmic plot from the slope of the fitted red line corresponds to $FD_{est} = 2.701$

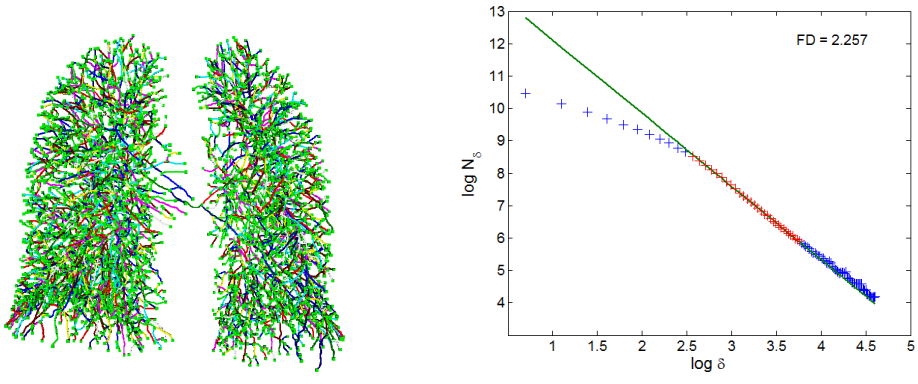

(a) (b)

Figure 4.5: (a) 3D rendering of lung vessel centerlines from one patient (b) double logarithmic plot of the number of non-empty boxes N_δ versus the box size δ. The slope of the fitted green line corresponds to the fractal dimension.

4.2 Tortuosity

Another quantifiable property of the vessels is their tortuosity, which is a readout of twistedness [8]. Vessels with high tortuosity are bent ("C"- or "S"-shape) and full of twists. The distance metric (DM) is a very common measure, which provides a ratio of the actual path length d_l to the linear distance between curve endpoints d_e. We use for tortuosity quantification of our vessel segments. One disadvantage of the DM is, that it is insensitive to the number of twists (related to the frequency) with which a vessel bends. More sophisticated measures like the sum of angle metric (SOAM [8]) do not have this drawback. However, the vessels in the lung that we are examining, show no high bending frequencies (at most C- or S-shape) and thus the more simple DM is sufficient to characterise them.

4.2.1 Distance Metric Computation

From the extracted vessel tree, see Section 2.3.7, we compute the actual length d_l of each vessel segment and divide it with the Euclidean distance between the endpoints d_e (Figure 4.6), resulting in a dimensionless number. Completely straight vessels will give a value of 1, highly bent and twisted vessels show high DM values. To find one value characterising the state of the whole vessel tree, we fitted an exponential curve to the histogram of the DM values. The parameter for the exponential fit μ, which is equivalent to the mean DM, is taken for quantitative analysis.

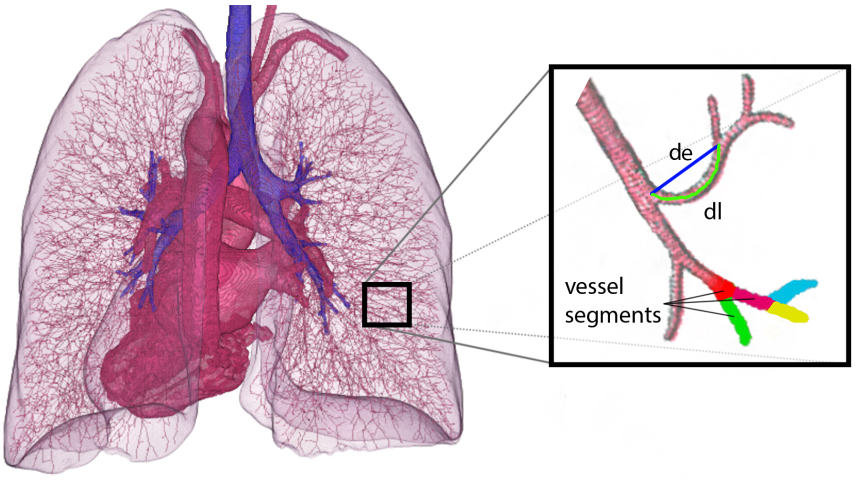

Figure 4.6: 3D Rendering of the lung, vessel centerlines (red), the heart (red) and the airways (blue). Inset shows the computation of the distance metric. The length of the vessel segment is divided by the Euclidean distance between the two endpoints, $DM = \frac{d_l}{d_e}$

4.2.2 Experiments and Results

Figure 4.7 shows the error of the exponential fit for all patients in our cohort. In Table 4.1 all results are listed.

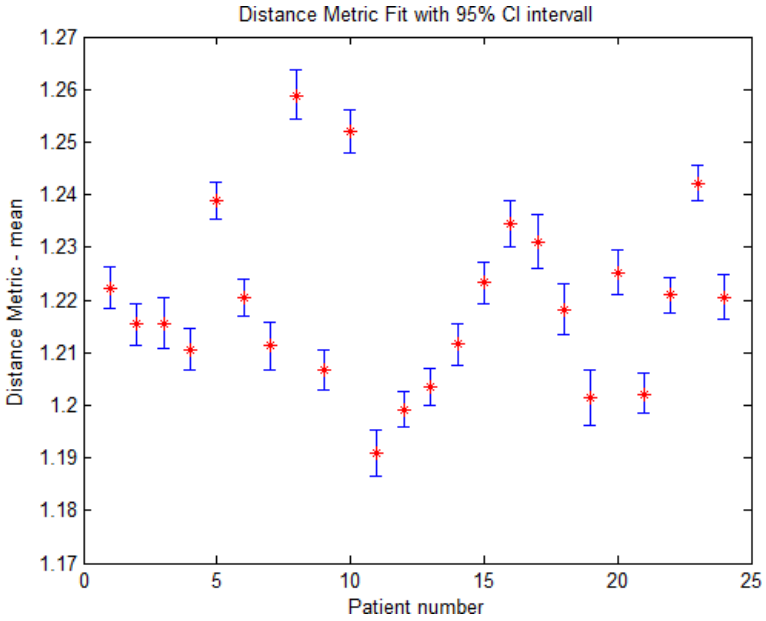

Figure 4.7: DM for all patients from the PH study cohort, including the 95% confidence interval of the fit.

Table 4.1: Values of the fractal dimension and the distance metric for all 24 patients from the clinical PH study.

Patient number	**Fractal dimension**	**Distance metric**
01	2.3763	1.24732
02	2.2901	1.21819
03	2.2667	1.23098
04	2.3339	1.23442
05	2.3896	1.22328
06	2.3994	1.2116
07	2.4313	1.20336
08	2.4221	1.19916
09	2.3225	1.252
10	2.3743	1.20667
11	2.2776	1.25885
12	2.3251	1.21123
13	2.4361	1.22042
14	2.3532	1.23878
15	2.3583	1.21047
16	2.3107	1.21557
17	2.3187	1.21535
18	2.3824	1.22224
19	2.358	1.2204
20	2.4133	1.24222
21	2.376	1.20214
22	2.2903	1.22517
23	2.2898	1.27318
24	2.212	1.2013
mean ± SD	2.35 ± 0.06	1.224 ± 0.019
(range)	(2.21 - 2.44)	(1.199 - 1.273)

Chapter 5

Clinical Application

Contents

Our clinical application is the non-invasive detection of pulmonary hypertension (PH) in patients from a clinical pilot study. Pulmonary hypertension is a type of disease presenting high blood pressure in the lung arteries and is defined as a mean pulmonary artery pressure (mPAP) $\geq$ 25 mmHg [18]. In severe cases, PH leads to a markedly decreased exercise tolerance and ultimately heart failure due to the high load in the right heart. The diagnostic marker for pulmonary hypertension is the mPAP, which is determined during invasive right-heart catheterisation (RHC) [54]. A non-invasive alternative to RHC would be beneficial for diagnosis of PH. Our hypothesis is, that the pulmonary vascular tree shows quantifiable differences between patients with and without PH. We correlate the readouts calculated from the vascular tree (distance metric, fractal dimension and number of vessel segments) with the patient's clinical parameters obtained during right heart catheterization.

5.1 Correlation with Clinical Parameters

24 patients (female:male = 14:10) were examined during this clinical pilot study, which was performed at the Ludwig Boltzmann Institute for Lung Vascular Research, Graz. Patient characteristics are listed in Appendix C. The patient group consisted of 18 patients with PH (4 with idiopathic pulmonary arterial hypertension (IPAH), 5 with pulmonary arterial hypertension other than IPAH, 2 with PH associated with lung disease, 7 with chronic

thromboembolic pulmonary hypertension) and 6 patients without PH (4 with systemic sclerosis, 1 with interstitial lung disease and 1 patient, who presented without PH after pulmonary endarterectomy).

Statistical analysis was performed in GraphPad Prism (Version 5.04, GraphPad Software, Inc., La Jolla, California) with Pearson correlation; differences between PH and non-PH patients were determined with Students t-test. Receiver-operator analysis was used to determine the conclusiveness of the parameters to determine the presence of PH. We considered p-values $p \leq 0.05$ as significant.

We found a correlation between mean pulmonary artery pressure (mPAP) and the distance metric (DM) of $r = 0.69$ (Figure 5.1a). As expected, there was a correlation of DM with the pulmonary vascular resistance (PVR; $r = 0.66$, Figure 5.1b) as this parameter strongly correlates with mPAP. The receiver operator curves showed a discriminative power of DM. The area under the curve (AUC) was 0.87 (sensitivity: 0.72, specificity: 0.83, cut-off value: > 1.202, Figure 5.2). There was a significant difference between the DM of patients with and without PH (Table 5.1). The mean value of the 3D fractal dimension in our patient cohort was 2.35 (range $2.21 - 2.44$, Table 5.1), which is in good agreement with previously reported values from similar studies [34]. However, there was no correlation of FD neither with mPAP nor with PVR which are the main diagnostic parameters of PH (Figure 5.3a,b).

Moreover, beside the main diagnostic parameters, there was a correlation of DM with other hemodynamic parameters determined during RHC, like the difference between arterial and venous oxygen content ($AVDO_2$, $r = 0.57$, Figure 5.4a) or arterial ($artSO_2$, $r = -0.67$, Figure 5.4c) or venous oxygen saturation ($venSO_2$, $r = -0.6$, Figure 5.4e). Finally, there was no correlation with age or body surface area (BSA), showing the specificity of the distance metric (Table 5.2). Interestingly, in the case of fractal dimension we obtained a weak correlation with $artSO_2$ ($r = 0.44$), but no other parameters correlated (Figure 5.4b, d, f). Despite our expectations, neither the distance metric nor the fractal dimension showed correlation with disease type (Figure 5.6).

The number of vessel segments extracted from the CT dataset does not correlate with any parameter (mPAP, PVR, $AVDO_2$, $artSO_2$ or $venSO_2$, Figure 5.5). This shows the robustness of the vessel detection algorithm, and that the other readouts are not influenced by a different number of detected vessels.

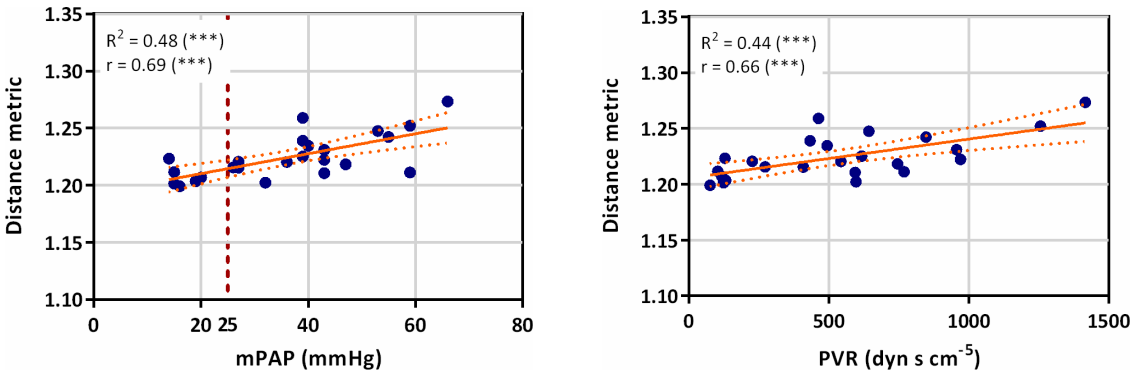

(a) (b)

Figure 5.1: Correlation of distance metric(DM) with (a) mean pulmonary artery pressure (mPAP), and (b) pulmonary vascular resistance (PVR; R = linear correlation coefficient, r = Pearson correlation coefficient, **/*** $p < 0.01/0.001$).

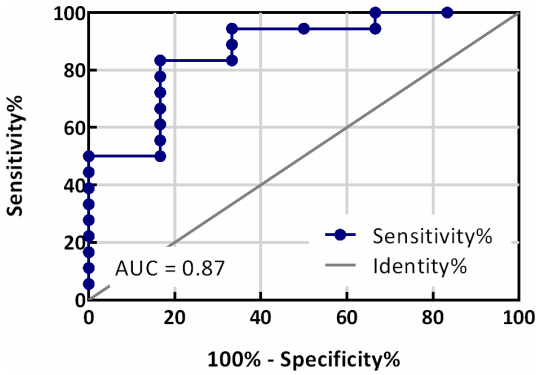

Figure 5.2: Receiver-operator-characteristic curve for DM determining mPAP > 25 mmHg (AUC: area under the curve).

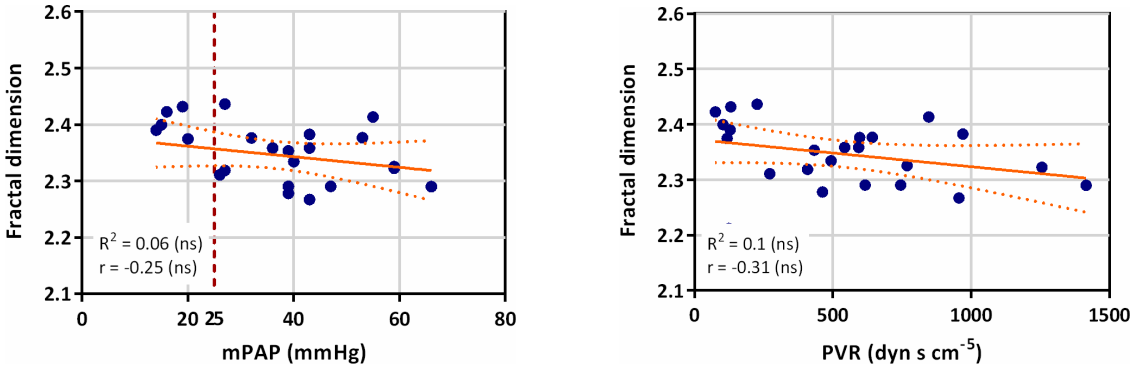

(a) (b)

Figure 5.3: Correlation of fractal dimension (FD) with (a) mean pulmonary artery pressure (mPAP), and (b) pulmonary vascular resistance (PVR; R = linear correlation coefficient, r = Pearson correlation coefficient, ns - not significant).

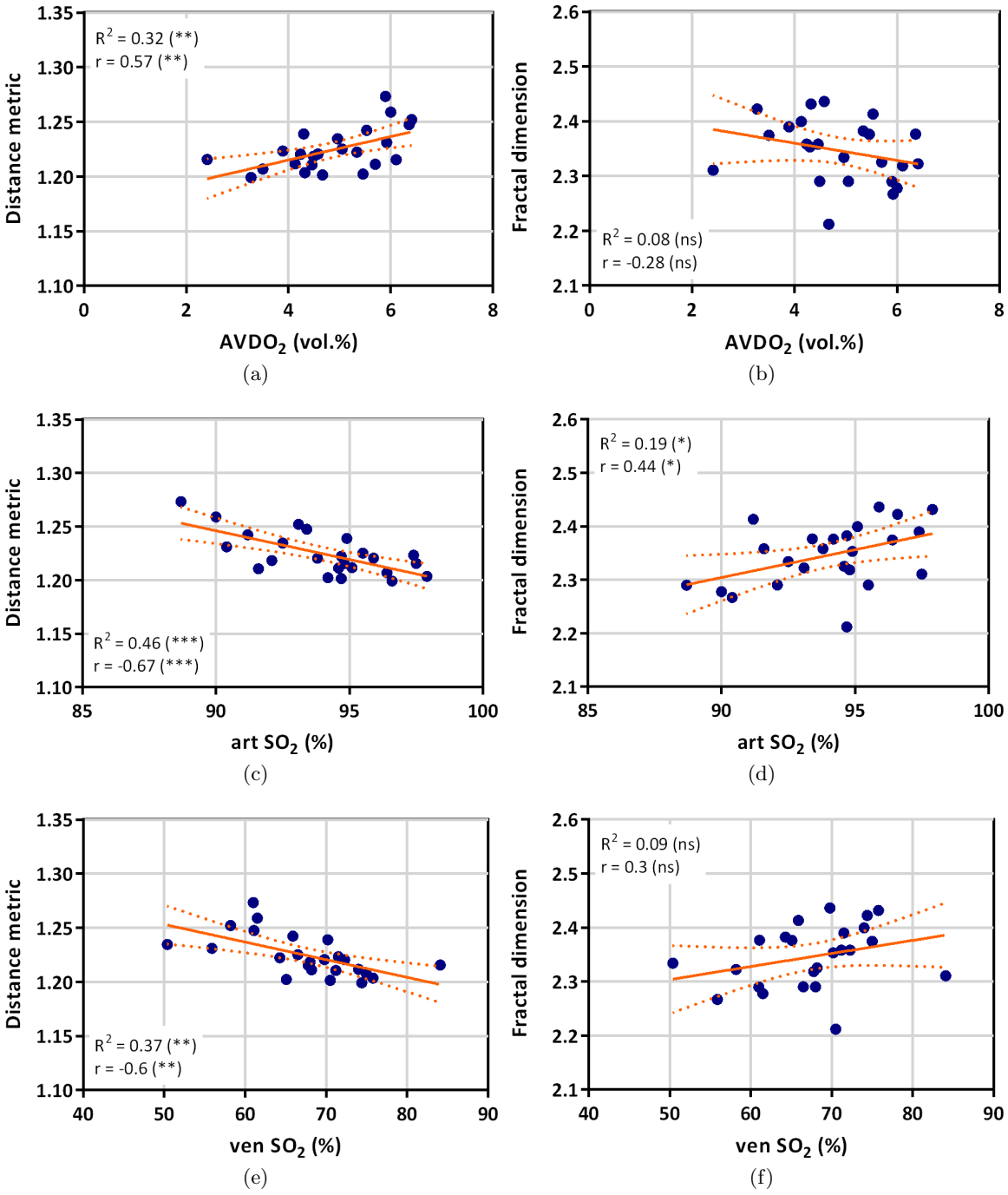

Figure 5.4: Correlation of distance metric (DM) (a, c, e) and 3D fractal dimension (b, d, f) with arterio-venous difference in oxygen content ($AVDO_2$: a, b), arterial ($artSO_2$: c, d) and venous ($venSO_2$: e, f) saturation of oxygen (R = linear correlation coefficient, r = Pearson correlation coefficient, */**/***/ns $p < 0.05/0.01/0.001$/notsignificant).

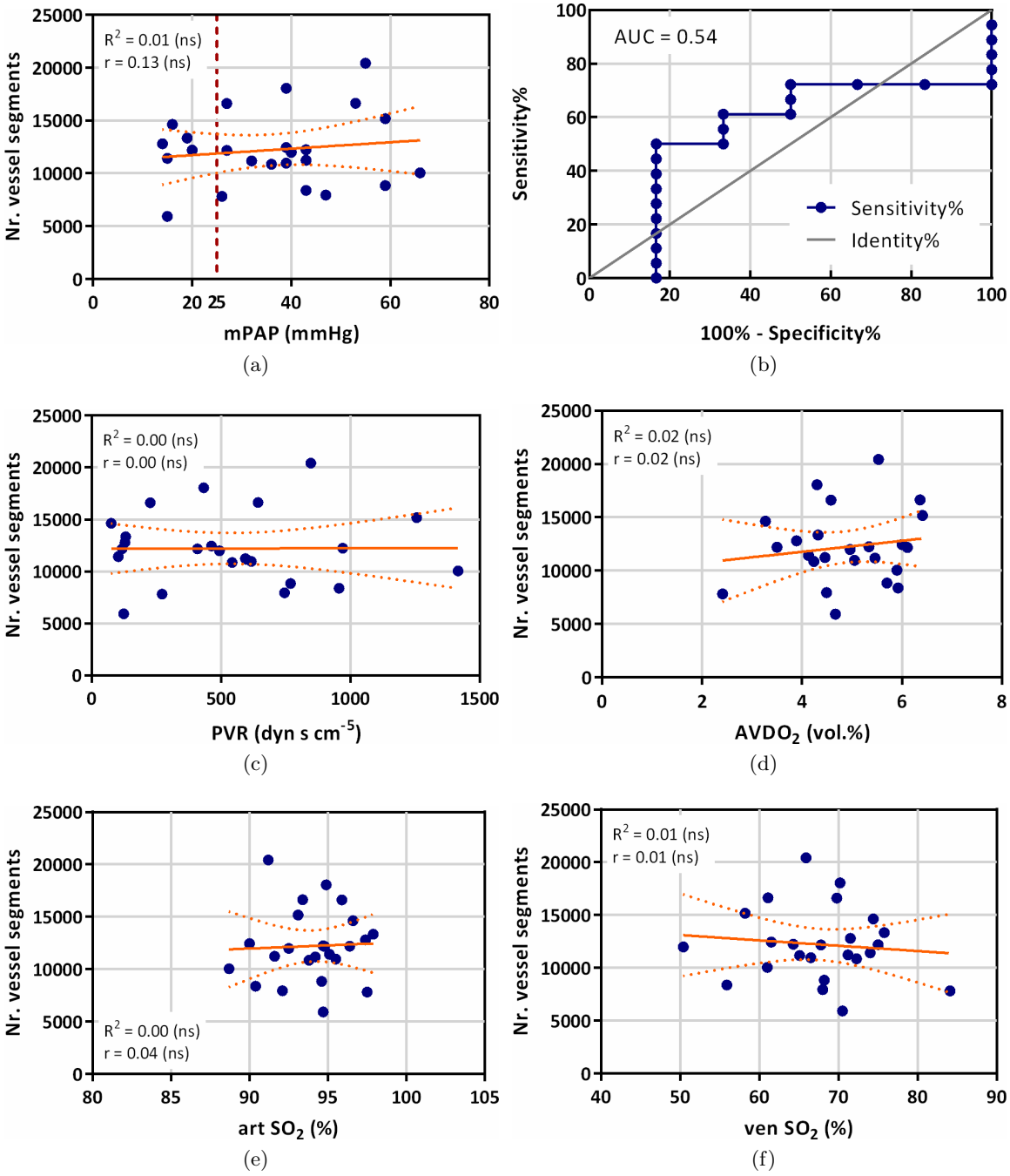

Figure 5.5: Correlation of number of vessel segments with mean pulmonary artery pressure (mPAP, a), ROC curve (b), pulmonary vascular resistance (PVR, c), arterio-venous difference in oxygen content ($AVDO_2$, d), arterial ($artSO_2$, e) and venous ($venSO_2$, f) saturation of oxygen (R = linear correlation coefficient, r = Pearson correlation coefficient, ns - not significant).

Table 5.1: Values of distance metric, fractal dimension and number of vessel segments.

Readout	All patients (n=24)	No PH (n=6)		PH (n=18)
Distance metric	1.224 ± 0.019 (1.199 – 1.273)	1.208 ± 0.009 (1.199 – 1.223)	*	1.230 ± 0.019 (1.223 – 1.273)
Fractal dimension	2.35 ± 0.06 (2.21 – 2.44)	2.37 ± 0.08 (2.21 – 2.43)	ns	2.34 ± 0.05 (2.27 – 2.44)
Nr. vessel segments	12233 ± 3575 (7815 – 20434)	11719 ± 3041 (5922 – 14642)	ns	12392 ± 3616 (7815 – 20434)

Data is presented as mean±SD (range). */ns: significant ($p < 0.05$)/ non-significant difference between PH and non-PH patients

Table 5.2: Correlations with patient clinical parameters (Pearson r and p-value) for $n = 24$ patients.

	Distance metric	Fractal dimension	Nr. vessel segments
mPAP	**0.69** (0.0002)	**-0.25** (0.23)	**0.13** (0.5)
PVR	**0.66** (0.0004)	**-0.31** (0.13)	**0.00** (0.9)
$AVDO_2$	**0.57** (0.0035)	**-0.28** (0.08)	**0.15** (0.4)
art SO_2	**-0.67** (0.0003)	**0.44** (0.03)	**0.04** (0.8)
ven SO_2	**-0.6** (0.0016)	**0.3** (0.14)	**-0.01** (0.6)
CO	**-0.18** (0.3)	**0.13** (0.53)	**-0.05** (0.7)
Age	**-0.34** (0.09)	**-0.17** (0.4)	**-0.37** (0.07)
BSA	**0.15** (0.4)	**-0.1** (0.6)	**-0.03** (0.8)

m*PAP: mean pulmonary artery pressure, PVR: pulmonary vascular resistance,* $AVDO_2$*: arterial-venous difference in oxygen content,* artSO_2*: arterial oxygen saturation,* venSO_2*: venous oxygen saturation, CO: cardiac output, BSA: body surface area after Dubois and Dubois*

5.2 Discussion and Limitations

In adult patients we have found that tortuosity instead of FD is correlated with pulmonary hypertension, proving the feasibility of non-invasive detection of PH with our vessel extraction and analysis algorithm using contrast enhanced CT. We found a significant correlation between mPAP and DM of $r = 0.69$ (Pearson correlation coefficient, $p < 0.01$). There was a significant difference between the DM of patients with and without PH (Table 5.1), thus enabling to discriminate the two groups on our data set of 24 patients. The correlations

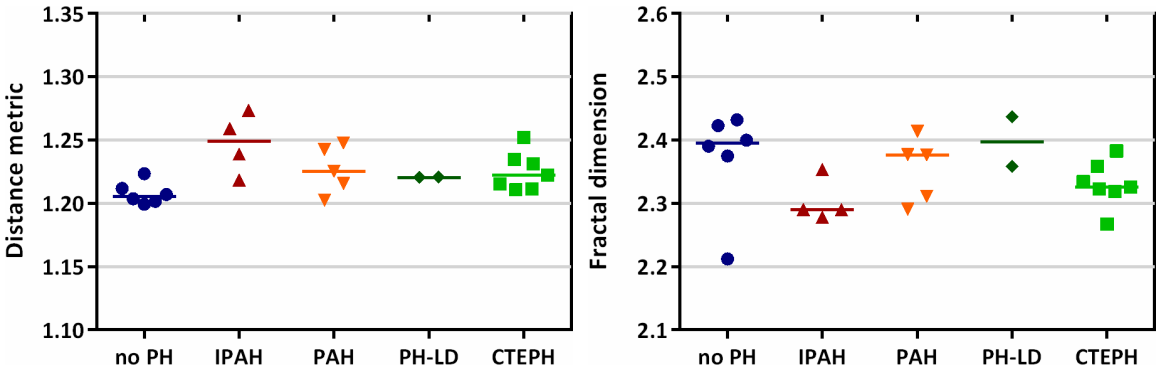

(a) (b)

Figure 5.6: Sub-group analysis of FD and DM based on disease type. Distribution of (a) distance metric (DM) and (b) fractal dimension (PH: pulmonary hypertension, CTEPH: chronic thromboembolic pulmonary hypertension, IPAH: idiopathic pulmonary arterial hypertension, PAH: pulmonary arterial hypertension other than IPAH, PH-LD: pulmonary hypertension associated with lung disease).

of FD reported in [23] are likely due to their patient cohort consisting of children, where the lung is still under development, changing its complexity. In [42] the correlations might be due to the MIP's used in the study. One of the limitations of this study is the small number of patients, which allows only a preliminary conclusion, despite considering a wide range of diseases. A large scale prospective study is necessary to determine the true benefits and constraints of this method. Further, due to radiation exposure one cannot test the repeatability of the method. This would be necessary to determine its ability for use in disease monitoring and follow-up examinations.

Chapter 6

Summary and Conclusion

We presented an automatic segmentation approach for pulmonary vessels from contrast-enhanced CT scans using a multi-scale vessel enhancement filter and including information from a lung- and airway-segmentation. The algorithm was tested on phantom data, the publicly available VESSEL12 challenge datasets as well as on 24 patients from a clinical pulmonary hypertension (PH) study. In case of the VESSEL12 challenge, our algorithm occupies a midfield position among all participating teams. Reasons for this performance of the algorithm are the optimization for the contrast-enhanced setup and for isotropic CT scans, which is not the case in all VESSEL12 dataset. We see room for improvement for the detection of very small vessels, which are currently hardly recognized. We achieved good segmentation results on our 24 patients from the clinical PH study. Because we had no ground truth for this dataset, we evaluated the segmentation results qualitatively together with the experts from the Ludwig Boltzmann Institute for Lung Vascular Research (LBI-LVR).

Due to a parallelized CUDA implementation, our whole vessel tree segmentation and centerline extraction has a run-time of about 10 minutes without the need for computing on reduced resolutions, thus enabling the potential use in daily clinical routine.

From the vessel segmentations, we created a graph representing the vascular structure and computed the fractal dimension and the distance metric, a measure for complexity and a measure for tortuosity of the vessels, respectively. In cooperation with the LBI-LVR we correlated the measures with actual clinical parameters of patients from the PH study. As an important outcome of our work, we showed that tortuosity is correlated with mean pulmonary arterial pressure and our vessel segmentation algorithm can detect the presence of PH.

Further improvement of the vessel detection algorithm could include a two-stage approach, first detecting large vessels and in a second step detecting small vessels. This could reduce wrong connections and even distinction between arteries and veins could be possible. The vessel connection step would also benefit from a segmentation of the lung lobes. For the clinical application of the detection of pulmonary hypertension, investigation of the distribution of the vessel radii could lead to new insights when correlating with clinical parameters. A large scale prospective study including additional 55 patients during the next two years to determine the true benefits and constraints of this method is currently planned at the LBI-LVR, and we intend to reproduce our results on this larger patient cohort.

Appendix A

List of Publications

Bibliography

[1] Helmberger, M., Pienn, M., Kovacs, G., Kullnig, P., Urschler, M., Olschewski, A., Olschewski, H., and Balint, Z. Fractal dimension of lung vessels negatively correlates with hemodynamics of patients. Poster presented at: *25th European Congress of Radiology (ECR)*; March 2013; Vienna, Austria

[2] Helmberger, M., Urschler, M., Pienn, M., Balint, Z., Olschewski, A., and Bischof, H. Pulmonary vascular tree segmentation from contrast-enhanced ct images. In: *Proceedings of the 37th Annual Workshop of the Austrian Association for Pattern Recognition (OEAGM/AAPR)*; Piater, J. and Rodriguez-Sanchez, A. (Eds), Innsbruck (2013) [Oral Communication].

[3] Helmberger, M., Urschler, M., Balint, Z., Pienn, M., Olschewski, A., and Bischof, H. Tortuosity of Pulmonary Vessels Correlates with Pulmonary Hypertension. In: *Proc. Medical Image Understanding and Analysis (MIUA)*; Birmingham (2013) [Oral Communication].

Appendix B

Framework Setup

The algorithm was implemented in C++ and tested under Ubuntu 12.04 LTS and Windows 7 64 bit. All open-source/free libraries used were compiled for 64 bit. As IDE Code Composer Studio was used under Ubuntu, and Visual C++ 2010 Express Edition under Windows (a problem with Express Edition and NVCC solved by Amitabh Mritunjai's answer: *http://stackoverflow.com/questions/2970493/cuda-linking-error-visual-express-2008-nvcc-fatal-due-to-null-configuratio,* Microsoft Windows SDK for Windows 7 is needed for Visual C++ express edition to be able to compile 64bit). Table B.1 lists all used open source libraries and tools.

Table B.1: Libraries and tools required for compilation of the framework

Library / Tool	**Remarks**
CMake 2.8.9	-
Boost 1.50	Precompiled library from http://boost.teeks99.com/ was used
Cuda 5.0	
CudaTemplates	http://cudatemplates.sourceforge.net/
ITK 3.20	Compiled with Cmake option ITK_USE_REVIEW
Coin 3.1.3	
Glew 1.9.0	
Quarter 1.0.0	
OpenSceneGraph 3.0.1	When using Visual Studio 2010, the /FORCE:MULTIPLE linker option has to be set

Appendix C

Patients Characteristics

The clinical PH study was approved by the local ethics committee and written informed consent was obtained from all 24 patients. All patients undergoing right heart catheterization (RHC) at the Department of Pulmonology between June 2011 and January 2013 with indication for diagnostic CT were included. The CT examination was carried out within one and 18 days of RHC, with a median of one day. No change in therapy occurred during these time points. Patients with and without pulmonary hypertension were included. Exclusion criteria were renal insufficiency, known adverse reactions against iodinated contrast material, a recent diagnostic CT and pregnancy.

Table C.1: Patient characteristics

Patient characteristics	All patients	No PH		PH
Number of patients	24	6		18
Female / male	14 / 10	4 / 2		10 / 8
Age [years]	60 ± 13 (27 – 76)	59 ± 9 (50 – 71)	ns	61 ± 15 (27 – 76)
BSA [m^2]	2.0 ± 0.3 (1.6 – 2.9)	2.0 ± 0.2 (1.8 – 2.3)	ns	2.0 ± 0.3 (1.6 – 2.9)
mPAP [mmHg]	36 ± 15 (14 – 66)	17 ± 2 (14 – 20)	***	43 ± 12 (26 – 66)
PAWP [mmHg]	9 ± 3 (3 – 15)	8 ± 2 (5 – 11)	ns	9 ± 3 (3 – 15)
CO [l/min]	4.5 ± 1.2 (2.9 – 7.8)	5.5 ± 1.5 (4.3 – 7.8)	*	4.2 ± 0.9 (2.9 – 5.7)
PVR [dyn s cm^{-5}]	540 ± 370 (80 – 1420)	110 ± 20 (80 – 130)	***	680 ± 320 (230 – 1420)
$AVDO_2$ [vol%]	4.9 ± 1.0 (2.4 – 6.4)	4.0 ± 0.5 (3.3 – 4.7)	**	5.2 ± 1.0 (2.4 – 6.4)
art SO_2 [%]	94 ± 2 (89 – 98)	96 ± 1 (95 – 98)	**	93 ± 2 (89 – 98)
ven SO_2 [%]	68 ± 7 (50 – 84)	74 ± 2 (71 – 76)	*	66 ± 7 (50 – 84)

Data are presented as mean±SD (range). The significance was tested with t-test. PH: pulmonary hypertension, BSA: body surface area after Dubois and Dubois, mPAP: mean pulmonary artery pressure, PAWP: pulmonary artery wedge pressure, CO: cardiac output, PVR: pulmonary vascular resistance, AVDO2: arterial-venous difference in oxygen content, art SO2: arterial oxygen saturation, ven SO2: venous oxygen saturation, */**/***/ns: significant ($p < 0.05/0.01/0.001$)/ non-significant difference between PH and non-PH patients

Bibliography

[1] Badesch, D. B., Raskob, G. E., Elliott, C. G., Krichman, A. M., Farber, H. W., Frost, A. E., Barst, R. J., Benza, R. L., Liou, T. G., Turner, M., Giles, S., Feldkircher, K., Miller, D. P., and McGoon, M. D. (2010). Pulmonary arterial hypertension: baseline characteristics from the REVEAL Registry. *Chest*, 137(2):376–387.

[2] Bauer, C. (2010). *Segmentation of 3D tubular tree structures in medical images*. PhD thesis, Graz University of Technology.

[3] Bauer, C. and Bischof, H. (2008). A novel approach for detection of tubular objects and its application to medical image analysis. In *Proceedings of the 30th DAGM symposium on Pattern Recognition*, pages 163–172, Berlin, Heidelberg. Springer-Verlag.

[4] Bauer, C., Pock, T., Sorantin, E., Bischof, H., and Beichel, R. (2010). Segmentation of interwoven 3d tubular tree structures utilizing shape priors and graph cuts. *Medical Image Analysis*, 14(2):172–184.

[5] Benisty, J. I. (2002). Cardiology patient page. Pulmonary hypertension. *Circulation*, 106(24):e192–194.

[6] Boskamp, T., Rinck, D., Link, F., Kummerlen, B., Stamm, G., and Mildenberger, P. (2004). New vessel analysis tool for morphometric quantification and visualization of vessels in CT and MR imaging data sets. *Radiographics*, 24(1):287–297.

[7] Bruijns, J. (2001). Fully-automatic branch labelling of voxel vessel structures. In *In Proc. Vision Modeling and Visuzalization 2001*, pages 341–350.

[8] Bullitt, E., Gerig, G., Pizer, S. M., Lin, W., and Aylward, S. R. (2003). Measuring tortuosity of the intracerebral vasculature from mra images. *IEEE Transactions on Medical Imaging*, 22:1163–1171.

[9] Day, M. and Topliss, C. (2011). Radiological diagnosis of degenerate change of the subtalar joint: A study comparing the reported degree of osteoarthritis in a plain radiograph when compared with a ct scan. *Journal of Bone & Joint Surgery, British Volume*, 93-B(SUPP IV):479.

[10] Dijkstra, E. W. (1959). A note on two problems in connexion with graphs. *Numerische Mathematik*, 1(1):269–271.

[11] Estrada, R., Tomasi, C., Cabrera, M. T., Wallace, D. K., Freedman, S. F., and Farsiu, S. (2012). Exploratory dijkstra forest based automatic vessel segmentation: applications in video indirect ophthalmoscopy (vio). *Biomed Opt Express*, 3(2):327–339.

[12] Falconer, K. (2003). *Fractal Geometry: Mathematical Foundations and Applications*. Wiley.

[13] Farid, H. and Simoncelli, E. P. (2004). Differentiation of discrete multidimensional signals. *IEEE Transactions on Image Processing*, 13:496–508.

[14] Frangi, A., Niessen, W., Vincken, K., and Viergever, M. (1998). Multiscale vessel enhancement filtering. In Wells, W., Colchester, A., and Delp, S., editors, *Medical Image Computing and Computer-Assisted Interventation MICCAI98*, volume 1496 of *Lecture Notes in Computer Science*, pages 130–137. Springer Berlin Heidelberg.

[15] Frangi, A. F., Niessen, W. J., Hoogeveen, R. M., van Walsum, T., and Viergever, M. A. (1999a). Model-based quantitation of 3-D magnetic resonance angiographic images. *IEEE Transactions on Medical Imaging*, 18(10):946–956.

[16] Frangi, A. F., Niessen, W. J., Hoogeveen, R. M., van Walsum, T., and Viergever, M. A. (1999b). Quantitation of vessel morphology from 3D MRA. In *MICCAI*, pages 358–367. Springer-Verlag.

[17] Frangi, A. F., Niessen, W. J., Nederkoorn, P. J., Elgersma, O. E. H., and Viergever, M. A. (2000). Three-dimensional model-based stenosis quantification of the carotid arteries from contrast-enhanced mr angiography. In *Proceedings of the IEEE Workshop on Mathematical Methods in Biomedical Image Analysis*, MMBIA '00, page 110, Washington, DC, USA. IEEE Computer Society.

[18] Galie, N., Hoeper, M. M., and Humbert, M. et al. (2009). Guidelines for the diagnosis and treatment of pulmonary hypertension. *Eur. Respir. J.*, 34(6):1219–1263.

[19] Gerig, G., Koller, T., Szekely, G., Brechbuhler, C., and Kubler, O. (1993). Symbolic description of 3-d structures applied to cerebral vessel tree obtained from mr angiography volume data. In *Information Processing in Medical Imaging*, volume 687 of *Lecture Notes in Computer Science*, pages 94–111. Springer Berlin Heidelberg.

[20] Glenny, R. W. (2011). Emergence of matched airway and vascular trees from fractal rules. *Journal of Applied Physiology*, 110(4):1119–1129.

[21] Glenny, R. W., Robertson, H. T., Yamashiro, S., and Bassingthwaighte, J. B. (1991). Applications of fractal analysis to physiology. *Journal of Applied Physiology*, 70(6):2351–2367.

[22] Graham, M., Gibbs, J., Cornish, D., and Higgins, W. (2010). Robust 3-d airway tree segmentation for image-guided peripheral bronchoscopy. *IEEE Transactions on Medical Imaging*, 29(4):982–997.

[23] Haitao, S., Ning, L., Lijun, G., Fei, G., and Cheng, L. (2011). Fractal dimension analysis of mdct images for quantifying the morphological changes of the pulmonary artery tree in patients with pulmonary hypertension. *Korean J Radiol*, 12:289–96.

[24] Hu, S., Hoffman, E., and Reinhardt, J. (2001). Automatic lung segmentation for accurate quantitation of volumetric x-ray ct images. *IEEE Transactions on Medical Imaging*, 20(6):490–498.

[25] Hua, P., Qi, S., Sonka, M., Hoffman, E., and Reinhardt, J. (2011). Segmentation of pathological and diseased lung tissue in ct images using a graph-search algorithm. In *IEEE International Symposiumon Biomedical Imaging: From Nano to Macro*, pages 2072–2075.

[26] Huang, W., Yen, R. T., McLaurine, M., and Bledsoe, G. (1996). Morphometry of the human pulmonary vasculature. *J. Appl. Physiol.*, 81(5):2123–2133.

[27] Hye Suk, K., Hyo-sun, Y., Kien Nguyen, T., and Sang Lee, G. (2007). Automatic lung segmentation in ct images using anisotropic diffusion and morphology operation. In *Computer and Information Technology, 2007. CIT 2007. 7th IEEE International Conference on*, pages 557–561.

[28] Itai, Y., Hyoungseop, K., Ishikawa, S., Katsuragawa, S., Ishida, T., Nakamura, K., and Yamamoto, A. (2005). Automatic segmentation of lung areas based on snakes and extraction of abnormal areas. In *17th IEEE International Conference onTools with Artificial Intelligence, ICTAI*, pages 381–386.

[29] Jiang, Y., Zhuang, Z., Sinusas, A. J., and Papademetris, X. (2010). Vascular tree reconstruction by minimizing a physiological functional cost. *Conf Comput Vis Pattern Recognit Workshops*, pages 178–185.

[30] Kirbas, C. and Quek, F. (2000). A review of vessel extraction techniques and algorithms. *ACM Computing Surveys*, 36:81–121.

[31] Krissian, K., Malandain, G., Ayache, N., Vaillant, R., and Trousset, Y. (2000). Model-based detection of tubular structures in 3d images. *Computer Vision and Image Understanding*, 80(2):130–171.

[32] Kruger, A. (1996). Implementation of a fast box-counting algorithm. *Computer Physics Communications*, 98:224–234.

[33] Lai, J. and Ye, M. (2009). Active contour based lung field segmentation. In *Intelligent Human-Machine Systems and Cybernetics, IHMSC*, volume 1, pages 288–291.

[34] Lang, S., Muller, B., Dominietto, M. D., Cattin, B. C., Zanette, I., Weitkamp, T., and Hieber, S. E. (2012). Three-dimensional quantification of capillary networks in healthy and cancerous tissues of two mice. *Microvasc Res*, 84(3):314–322.

[35] Lassen, B., van Rikxoort, E. M., Schmidt, M., Kerkstra, S., van Ginneken, B., and Kuhnigk, J. M. (2013). Automatic segmentation of the pulmonary lobes from chest CT scans based on fissures, vessels, and bronchi. *IEEE Trans Med Imaging*, 32(2):210–222.

[36] Lesage, D., Angelini, E., Bloch, I., and Funka-Lea, G. (2009). A review of 3d vessel lumen segmentation techniques: Models, features and extraction schemes. *Medical Image Analysis*, 13(6):819–845.

[37] Lo, P., van Ginneken, B., Reinhardt, J. M., Yavarna, T., de Jong, P. A., Irving, B., Fetita, C., Ortner, M., Pinho, R., Sijbers, J., Feuerstein, M., Fabijanska, A., Bauer, C., Beichel, R., Mendoza, C. S., Wiemker, R., Lee, J., Reeves, A. P., Born, S., Weinheimer, O., van Rikxoort, E. M., Tschirren, J., Mori, K., Odry, B., Naidich, D. P., Hartmann, I., Hoffman, E. A., Prokop, M., Pedersen, J. H., and de Bruijne, M. (2012). Extraction of airways from ct (exact'09). *Medical Imaging, IEEE Transactions on*, 31(11):2093–2107.

[38] Maeda, S., Kim, H., Tan, J. K., Ishikawa, S., Murakami, S., and Aoki, T. (2012). Nonrigid image registration method for thoracic ct images using vessel structure information. In *SMC*, pages 1413–1417. IEEE.

[39] Mandelbrot, B. (1967). How long is the coast of britain? statistical Self-Similarity and fractional dimension. *Science*, 156(3775):636–638.

[40] Masters, B. R. (2004). Fractal analysis of the vascular tree in the human retina. *Annual Review of Biomedical Engineering*, 6(1):427–452.

[41] Meiling, G., Qizhong, L., and Wang, L. (2006). Realizing the box-counting method for calculating fractal dimension of urban form based on remote sensing image. In *IEEEInternational Conference on Geoscience and Remote Sensing Symposium, IGARSS*, pages 1423–1426.

[42] Moledina, S., de Bruyn, A., Schievano, S., Owens, C. M., Young, C., Haworth, S. G., Taylor, A. M., Schulze-Neick, I., and Muthurangu, V. (2011). Fractal branching quantifies vascular changes and predicts survival in pulmonary hypertension: a proof of principle study. *Heart*, 97(15):1245–1249.

[43] Mortensen, E. N. and Barrett, W. A. (1995). Intelligent scissors for image composition. In *In Computer Graphics, SIGGRAPH Proceedings*, pages 191–198.

[44] Niemeijer, M. Van Ginneken, B. and D. Abramoff, M. (2009). A linking framework for pixel classification based retinal vessel segmentation. *Proc. SPIE 7262*.

[45] Notter, R. (2000). *Lung Surfactants: Basic Science and Clinical Applications*. Lung Biology in Health and Disease Series. Marcel Dekker Incorporated.

[46] Otsu, N. (1979). A threshold selection method from gray-level histograms. *IEEE Transactions on Systems, Man and Cybernetics*, 9(1):62–66.

[47] Pechin, L., van Ginneken, B., and de Bruijne, M. (2010). Vessel tree extraction using locally optimal paths. In *Biomedical Imaging: From Nano to Macro, 2010 IEEE International Symposium on*, pages 680–683.

[48] Pock, T., Beichel, R., and Bischof, H. (2005). A novel robust tube detection filter for 3d centerline extraction. In *Image Analysis*, volume 3540 of *Lecture Notes in Computer Science*, pages 481–490. Springer Berlin Heidelberg.

[49] Pu, J., Fuhrman, C., Good, W. F., Sciurba, F. C., and Gur, D. (2011). A differential geometric approach to automated segmentation of human airway tree. *IEEE Trans Med Imaging*, 30(2):266–278.

[50] Reinbacher, C., Pock, T., Bauer, C., and Bischof, H. (2010). Variational segmentation of elongated volumetric structures. In *The Twenty-Third IEEE Conference on Computer Vision and Pattern Recognition, CVPR*, pages 3177–3184. IEEE.

[51] Rudin, L. I., Osher, S., and Fatemi, E. (1992). Nonlinear total variation based noise removal algorithms. *Phys. D*, 60(1-4):259–268.

[52] Sethian, J. A. (1996). A fast marching level set method for monotonically advancing fronts. *Proc. Natl. Acad. Sci. U.S.A.*, 93(4):1591–1595.

[53] Shikata, H., McLennan, G., Hoffman, E. A., and Sonka, M. (2009). Segmentation of pulmonary vascular trees from thoracic 3d ct images. *Journal of Biomedical Imaging*, 24:1–11.

[54] Simonneau, G., Robbins, I., Beghetti, M., Channick, R., Delcroix, M., Denton, C., Elliott, G., Gaine, S., Gladwin, T., Jing, Z., Krowka, M., Langleben, D., Nakanishi, N., and Souza, R. (2009). Updated clinical classification of pulmonary hypertension. *Journal of the American College of Cardiology*, 54(1, Supplement):43–54.

[55] Sluimer, I., Schilham, A., Prokop, M., and van Ginneken, B. (2006). Computer analysis of computed tomography scans of the lung: a survey. *IEEE Trans Med Imaging*, 25(4):385–405.

[56] Sun, S., Bauer, C., and Beichel, R. (2012). Automated 3-d segmentation of lungs with lung cancer in ct data using a novel robust active shape model approach. *Medical Imaging, IEEE Transactions on*, 31(2):449–460.

[57] Szymczak, A., Stillman, A., Tannenbaum, A., and Mischaikow, K. (2006). Coronary vessel trees from 3d imagery: a topological approach. *Med Image Anal*, 10(4):548–559.

[58] Toyama, Y., Kobayashi, T., Nishiyama, Y., Satoh, K., Ohkawa, M., and Seki, K. (2005). CT for acute stage of closed head injury. *Radiat Med*, 23(5):309–316.

[59] Unger, M., Pock, T., Trobin, W., Cremers, D., and Bischof, H. (2008). Tvseg – interactive total variation based image segmentation. In *British machine vision conference (BMVC)*.

[60] Zhou, C., Chan, H. P., Sahiner, B., Hadjiiski, L. M., Chughtai, A., Patel, S., Wei, J., Ge, J., Cascade, P. N., and Kazerooni, E. A. (2007). Automatic multiscale enhancement and segmentation of pulmonary vessels in CT pulmonary angiography images for CAD applications. *Med Phys*, 34(12):4567–4577.